Patient-Derived Mutant Forms of NFE2L2/NRF2 Drive Aggressive Murine Hepatoblastomas

Huabo Wang[1], Jie Lu[1], Jordan A. Mandel[1], Weiqi Zhang[2], Marie Schwalbe[1,3], Joanna Gorka[1], Ying Liu[1,3], Brady Marburger[1,3], Jinglin Wang[1,4], Sarangarajan Ranganathan[5], Edward V. Prochownik[16,7,8,9]

[1]Division of Hematology/Oncology, UPMC Children's Hospital of Pittsburgh; [2]Tsinguhua University School of Medicine, Beijing, People's Republic of China; [3]The University of Pittsburgh School of Medicine; [1,4]Central South University Xiangya University Medical School, Changsha, People's Republic of China; [5]Department of Pathology, Cincinnati Children's Hospital, Cincinnati, OH; [6]The Department of Microbiology and Molecular Genetics, UPMC; [7]The Hillman Cancer Center, UPMC; [8]The Pittsburgh Liver Research Center, Pittsburgh, PA.

[9]Corresponding author:
Email: procev@chp.edu

Classification: Major classification: Biological Sciences
Minor classification: Medical Sciences

Key words: Hepatocellular carcinoma, Hippo, KEAP1, PAI-1, reactive oxygen species, Serpin E1, Warburg effect, Wnt

Author contributions

Conceived experiments: EVP, HW
Performed, analyzed and interpreted experiments: HW, JL, JW, MS, JG, JZ, EVP
Performed Bioinformatics: JAM, HW, YL, BM
Histologic interpretation: SR
Manuscript preparation: EVP, HW

Abstract

The pediatric liver cancer hepatoblastoma (HB) often expresses mutant forms of β-catenin and deregulates the Hippo tumor suppressor pathway. Murine HBs can be generated by co-expressing these β-catenin mutants and the constitutively active Hippo effector YAP^{S127A}. Some HBs and other human cancers also express mutant forms of NFE2L2/NRF2 (NFE2L2), a bHLH transcription factor that tempers oxidative and electrophilic stress. In doing so, NFE2L2 either suppresses or facilitates tumorigenesis in a context- and time-dependent manner. We show here that two patient-derived NFE2L2 missense mutants, L30P and R34P, markedly accelerate HB growth in association with widespread cyst formation, an otherwise uncommon feature of human HB. Surprisingly, we found that any two members of the mutant β-catenin-YAP^{S127A}-L30P/R34P triad were tumorigenic, thus providing direct evidence for NFE2L2's role as an oncoprotein. Each tumor group displayed distinct features but shared a similarly deregulated set of 22 transcripts, 10 of which perfectly correlated with survival in human HBs. 17 transcripts also correlated with survival in multiple other adult cancers. One of the most highly deregulated transcripts encoded serpin E1, a serine protease inhibitor with roles in fibrinolysis, tumor growth and extracellular matrix formation. The combination of mutant β-catenin, YAP^{S127A} and Serpin E1, while not accelerating tumor growth or generating cysts, did promote the wide-spread necrosis previously associated with the cysts of mutant β-catenin-YAP^{S127A}-L30P/R34P tumors. These findings establish the direct oncogenicity of NFE2L2 mutants and identify key transcripts, including serpin E1, that drive specific HB features.

Significance statement

Hepatoblastomas (HBs) often accumulate nuclear mutant β-catenin and yes-associated protein (YAP) and sometimes deregulate NFE2L2. Patient-associated NFE2L2 mutants accelerate β-catenin+YAP^{S127A}-driven tumorigenesis and generate numerous cysts with areas of adjacent necrosis. NFE2L2 mutants are also directly oncogenic when co-expressed with mutant β-catenin or YAP. In tumors arising from various β-catenin/YAP/NFE2L2 combinations, we identified 22 common transcripts, many of which correlated with survival in other cancers. Over-expression of one of these transcripts, serpin E1, recapitulated the necrosis but not the cysts associated with mutant β-catenin-YAP-NFE2L2 co-expression. These studies identify NFE2L2 as an oncoprotein and describe a minimal set of genes responsible for different tumor behaviors.

Introduction

Hepatoblastoma (HB), the most common pediatric liver cancer, is usually diagnosed before the age of 3 years. Factors negatively impacting long-term survival include older age, low levels of circulating α-fetoprotein, certain histologic subtypes and transcriptional profiles (1, 2). Approximately 80% of HBs harbor acquired missense or in-frame deletion mutations in the β-catenin transcription factor. These represent the most common genetic abnormality and are responsible for β-catenin's nuclear accumulation (3). A similar proportion of HBs also deregulate the Hippo signaling pathway and aberrantly accumulate its terminal effector YAP (yes-associated protein) in their nuclei as well (3, 4).

Unlike most oncoproteins, whose activating mutations tend to be quite restricted, those in β-catenin are highly diverse (3-6). Most impair the cytoplasmic interaction between the adenomatous polyposis coli complex that normally phosphorylates β-catenin and licenses its rapid proteasome-mediated degradation (3-6). These now stabilized β-catenin mutants enter the nucleus, associate with members of the Tcf/Lef family of transcriptional co-regulators, alter the expression of known oncogenic drivers such as c-Myc and Cyclin D1 and drive tumorigenesis (3, 4, 6-8). Hydrodynamic tail vein injection (HDTVI) of Sleeping Beauty (SB) plasmids encoding a patient-derived 90 bp in-frame N-terminal deletion of β-catenin [Δ(90)] and YAP^{S127A}, a nuclearly-localized YAP mutant, efficiently promote HB tumorigenesis whereas neither Δ(90) nor YAP^{S127A} alone is tumorigenic (4, 7, 8).

Different β-catenin mutants influence the growth rate, histology, metabolism and transcriptional profiles of the tumors they generate in distinct ways (7, 9). For example, mice with Δ(90)-driven HBs have a median survival of ~11-13 wks, show the "crowded fetal" histopathologic pattern typical of the most common human HB subtype and differentially express ~5300 transcripts relative to normal liver (1, 2, 7, 8). In contrast, tumors generated by the deletion mutant Δ(36-53) have longer median survival, greater histologic heterogeneity and differentially express >6400 transcripts (7). The basis for these differences and those associated with other β-catenin mutants are complex and driven by this transcriptional diversity that reflects each mutant's level of expression, the efficiency of its nuclear localization and its transcriptional potency (7).

Unlike adult cancers, which display enormous genetic diversity. pediatric cancers in general and HBs in particular demonstrate many fewer changes (10, 11). However, in addition to β-catenin mutations, ~5-10% of human HBs harbor recurrent missense mutations in the *NFE2L2/NRF2* (Nuclear factor, erythroid 2-like 2) gene and as many as 50% have copy number increases (12, 13). Similar findings have been reported in adult cancers, most notably ovarian, non-small cell lung and head and neck cancers and correlate with shorter survival (14-16). HBs with *NFE2L2* mutations reportedly have shorter survival, although how this was influenced by underlying β-catenin mutational differences was not considered (12, 13). Our transcriptional profiling of 45 murine HBs generated by eight patient-derived β-catenin mutants identified an *NFE2L2* point mutation (L30P) in one tumor that grew more rapidly than others in its cohort (7). Collectively, these findings present largely anecdotal reckonings of NFE2L2's role in HB, which cannot be further evaluated due to small case numbers and the above-mentioned biological and molecular heterogeneity.

As a member of the "Cap 'n' Collar" bZIP transcription factor family, NFE2L2 mediates adaptive responses to oxidative, electrophilic and xenobiotic stress and bears regulatory similarities to β-catenin (16, 17). NFE2L2 normally forms a cytoplasmic complex with Kelch-like ECH-associated protein 1 (KEAP1) that requires two short NFE2L2 segments known as the ETGE and DLG domains (16, 17). NFE2L2-KEAP1 complexes interact with Cullin 3, an E3 ubiquitin ligase that targets NFE2L2 for proteosomal degradation, thus ensuring low basal expression (18-20). The afore-mentioned stresses prompt the oxidation of multiple KEAP1 cysteine thiol groups that maintain the complex's integrity (18-20). Dissociated and now stabilized NFE2L2 is thus translocated to the nucleus where it heterodimerizes with members of the small Maf family of bZIP transcription factors and binds to anti-oxidant response elements (AREs) in several hundred target genes. Their products restore redox balance, metabolize xenobiotics, counter stress and apoptosis, regulate metabolic pathways such as the pentose phosphate shunt and maintain genomic and mitochondrial integrity (16, 20-22). Most cancer-associated NFE2L2 mutations, including L30P, reside within or near the ETGE or DLG domains and abrogate the association with KEAP1 thereby leading to constitutive NFE2L2 nuclear translocation and target gene engagement (15, 16, 18). Alternatively, copy number differences in the *NFE2L2* and *KEAP1* genes create stoichiometric imbalance between their encoded proteins and allow for a similar nuclear accumulation of wild-type NFE2L2 (23, 24).

NFE2L2 target gene products buffer the reactive oxygen species (ROS)- and electrophile-mediated genotoxicity that contributes to cancer initiation and evolution. This is supported by findings in *nfe2l2-/-* mice, which are prone to carcinogen-mediated liver, bladder and stomach cancers (25, 26). NFE2L2 target gene products that scavenge ROS include peroxiredoxins, thioredoxin and thioredoxin reductase whereas other products detoxify and/or promote the excretion of compounds containing α,β–unsaturated carbonyl, epoxide and quinone moieties and their metabolites (27-29).

In contrast to its tumor suppressor-like attributes, NFE2L2 mutation or over-expression may also facilitate the growth of previously established tumors via the same pathways and mechanisms described above. Proliferating tumor cells generate ROS as a consequence of metabolic hyperactivity, mitochondrial dysfunction and over-expression of ROS-generating oncoproteins such as Myc and Ras (30-32). Although ROS abet growth factor-mediated proliferation and confer other long-term benefits when expressed at low levels (33, 34), these advantageous effects are limited by oxidant-mediated macromolecular damage, cellular senescence and/or apoptosis when these levels are exceeded or otherwise poorly regulated (30, 31). NFE2L2-induced ROS scavengers may increase cancer cells' ability to survive abnormally high levels of oxidative stress, thus permitting otherwise unattainable levels of oncogene-stimulated metabolism, proliferation and aggressiveness to be achieved. Some NFE2L2 target gene products unrelated to those involved in redox state regulation also specifically benefit tumor growth, angiogenesis and survival (35-39). These effects may be particularly prominent in tumors with mutated TP53, which, in addition to its well-known

role in DNA repair and apoptosis, also suppresses a subset of NFE2L2-responsive genes (40). NFE2L2 may also inhibit the expression of certain pro-inflammatory and ROS-generating cytokines such as IL-1β, IL-3, and TNF-α (41). Finally, metastatic propensity may be facilitated in tumor cells as a consequence of NFE2L2 activation given that an oxidized environment is rate-limiting for this behavior in several models (42, 43).

Mindful of these considerations, we show here that two patient-derived NFE2L2 missense mutants, L30P and R34P, each dramatically accelerates hepatic tumorigenesis when co-expressed with β-catenin mutants and YAP^{S127A}. The tumors were also found to possess innumerable fluid-filled cysts, a rare HB attribute (44), and were associated with large areas of adjacent necrosis. The exceedingly rapid growth of β-catenin+YAP^{S127A} +L30P/R34P tumors appears to result from their more robust anti-oxidant response and a more conducive metabolic environment. L30P and R34P, rather than simply facilitating established tumor growth, were also transforming when co-expressed with either Δ(90) β-catenin or YAP^{S127A} alone, thus establishing NFE2L2 mutants as *bona fide* oncoproteins. RNA-seq of HBs expressing each possible Δ(90), YAP^{S127A} and L30P/R34P combination identified an overlapping "core" set of 22 common and similarly regulated target genes whose expression correlated with long-term survival in HBs and numerous other cancers. While not affecting tumor growth or promoting cyst formation when co-expressed with Δ(90) and YAP^{S127A} one of these transcripts, encoding the serine protease inhibitor serpin E1, generated tumors with widespread necrosis thereby supporting the idea that these 22 common transcripts cooperatively contribute in distinctive ways to various tumor phenotypes.

Results

NFE2L2 mutants accelerate hepatic tumorigenesis. Numerous patient-derived β-catenin mutations and even wild-type (WT) β-catenin itself are tumorigenic in collaboration with YAP^{S127A} (4, 7-9). However, tumor features and global gene expression profiles are strongly dictated by the β-catenin mutant's identify (8, 9). Despite these differences, endogenous NFE2L2 transcripts were equivalently up-regulated (ca. two-fold) in all tumor groups relative to those of control livers (*SI Appendix* Fig. 1A). Similar induction was observed in slower growing Δ(90)+YAP^{S127A} tumors lacking Myc, ChREBP or Myc+ChREBP (8, 44). Like Myc, ChREBP is a bHLH-ZIP transcription factor that regulates a subset of Myc target genes involved in carbohydrate and lipid metabolism and ribosomal biogenesis (45). These results indicate that NFE2L2 is induced equally in murine HBs regardless of growth rates, other metabolic or molecular features or Myc and ChREBP status. In contrast, all tumors and livers expressed similar levels of KEAP1 transcripts (*SI Appendix* Fig. S1B).

Recurrent *NFE2L2* missense mutations occur in 5-10% of HBs and at higher frequencies in other cancers (12-15, 24). Although correlated with inferior survival, this has not been directly demonstrated (12, 13, 16). Using HDTVI, we transfected mouse livers with SB vectors encoding Δ(90)+YAP^{S127A}, with or without WT-NFE2L2 or HB-associated L30P and R34P missense mutants (12). As previously reported, mice with Δ(90)+YAP^{S127A} tumors had median survival of ~11-13 wk (Fig. 1A) (4, 7, 8, 46), which was unaltered by co-injection with WT NFE2L2. In contrast L30P and R34P co-expression each significantly shortened survival (Fig. 1A).

Unexpectedly, all L30P/R34P-expressing tumors contained numerous, fluid-filled cysts that extended deep into the parenchyma and were associated with large areas of adjacent necrotic tissue (Fig. 1B-D). The tumors also showed the crowded fetal pattern previously described in Δ(90)+YAP^{S127A} neoplasms (4, 7, 8, 46) (Fig. 1D and *SI Appendix* Fig. S2). Cells lining the cysts were indistinguishable from tumor cells indicating that they were derived from epithelium as is typical of benign cysts (Fig. 1E and *SI Appendix* Fig. S2) (47-49). These lining cells also showed the intense nuclear staining characteristic of mutant β-catenin but did not stain for the endothelial marker CD34 (Fig. 1E and data not shown). In no case did control Δ(90)+YAP^{S127A} tumors contain cysts or significant areas of necrosis.

In association with YAP^{S127A}, the β-catenin missense mutant R582W generates slowly-growing tumors that more closely resemble hepatocellular carcinomas (HCCs) with some HB elements (7). L30/R34 also accelerated the growth of these tumors and promoted the formation of numerous cysts (Fig. 1F&G and *SI Appendix* Fig. S3).

L30P and R34P are stabilized, localized to the nucleus and alter metabolic and redox states. L30P and

R34P were modestly but reproducibly over-expressed relative to WT or endogenous NFE2L2 protein in livers and Δ(90)+YAP^{S127A} tumors, whereas endogenous KEAP1 expression was equal across all cohorts (Fig. 2A and *SI Appendix* Fig. S1B). The Glut1/Slc2a1 glucose transporter was prominently expressed in L30P/R34P tumors (Fig. 2A) and was consistent with their more rapid growth and greater reliance on Warburg-type respiration that typifies many tumors, including HB (7, 8, 46, 50). Further consistent with this and the reduced β-fatty acid oxidation (β-FAO) of HBs (7, 8, 46, 49), all tumors, but particularly those in L30P/R34P cohorts, expressed lower levels of carnitine palmitoyltransferase I (Cpt1a), β-FAO's rate-limiting enzyme (51). The majority of NFE2L2, regardless of its origin, localized to nuclei in contrast to cytoplasmicallly-localized KEAP 1 (Fig. 2B). Thus unlike cell lines, in which NFE2L2 is usually cytoplasmic (16, 52, 53), most NFE2L2 in livers and HBs is nuclear, regardless of mutational status. This may reflect both the liver's normal function as an active site of xenobiotic metabolism as well as tumor redox imbalance (54, 55).

To assess the consequences of L30P/R34P expression on metabolic functions relevant to HB growth, we examined oxygen consumption rates (OCRs) of partially purified mitochondria in response to TCA cycle substrates. Consistent with the afore-mentioned switch from oxidative phosphorylation (Oxphos) to Warburg-type respiration, total OCRs and individual contributions of Complex I and Complex II were reduced across all tumors groups relative to livers (Fig. 2C-E). In further keeping with previous observations (7, 8, 46, 56), all tumors increased their pyruvate response while suppressing their glutamate response (Fig. 2F and G).

HBs suppress β-FAO as they shift to Warburg-type respiration and as more stored hepatic lipid is mobilized for *de novo* membrane synthesis (7, 8, 46). Consistent with this, all tumors, regardless of NFE2L2 status, similarly down-regulated β-FAO (Fig. 2H). Thus, based on these studies, the distinguishing features of L30P/R34P tumors are their markedly faster growth rates and more prominent expression of Glut1.

Many tumors, including murine HBs, reduce their mitochondrial mass as determined by mitochondrial DNA (mtDNA) levels (7, 8, 46). This was also observed in all tumor cohorts (Fig. 2I).

We next generated tumors that expressed redox-sensitive forms of GFP that localize to the cytoplasm or mitochondrial matrix (cyto-roGFP and mito-roGFP, respectively) (57). Primary tumor cells were cultured for several days *in vitro* and briefly exposed to H_2O_2 while continuously monitoring their recovery by live-confocal microscopy. Δ(90)+YAP^{S127}+WT-NFE2L2 cells recovered somewhat more rapidly than Δ(90)+YAP^{S127A} cells but the recovery was significantly accelerated in tumor cells expressing L30P/R34P (Fig. 2J).

L30P/R34P are tumorigenic in combination with either Δ(90) or YAP^{S127A}. The acceleration of Δ(90)+YAP^{S127A}-driven tumorigenesis by L30P/R34P (Fig. 1A) raised questions regarding the latters' role(s) in promoting transformation. While no individual vector was oncogenic (Fig. 3A and refs. 4, 8), L30P and R34P each generated tumors when co-expressed with either Δ(90) or YAP^{S127A} with survivals comparable to those of the R582W+YAP^{S127A} cohort (Figs. 1F and 3A and ref. 7). These findings indicated that any pairwise combination of the Δ(90)/YAP^{S127A}/L30P/R34P triad is oncogenic. Histologically, Δ(90)+L30P/R34P tumors were highly differentiated whereas YAP^{S127A}+L30P/R34P tumors more closely resembled HCC with HB-like features (Fig. 3B, and *SI Appendix* Fig. S4) (7, 8, 47, 56).

Metabolically, YAP^{S127A}+L30P/R34P tumors resembled those previously described (Fig. 3C-E and refs. 7, 8, 46) whereas Δ(90)+L30P/R34P tumors were distinct, with higher total OCRs and Complex I and II activities. Moreover, rather than the reciprocal relationship between β-FAO and pyruvate consumption and lower levels of glutamate consumption previously documented in HBs and Myc-driven HCCs (Fig. 2F&H and refs. 7, 8, 39, 46), all activities were increased in Δ(90)+L30P/R34P tumors (Fig. 3 F-H). Rather than being due to an increase in mitochondrial efficiency, these activities were associated with increased mitochondrial mass that exceeded even that of control livers (Fig. 3I).

The expression of key components of the above pathways, while complex, uniquely reflected the identities of each cohort (Fig. 3J). For example, expression of the pyruvate dehydrogenase α1 catalytic subunit (PDHα1) was slightly lower in Δ(90)+YAP^{S127A} tumors than in livers (7, 8, 46). However, Ser$_{293}$-phosphorylated PDHα1 (pPDHα1) was markedly reduced in the former, indicating PDH activation and thus likely explaining the higher OCR response to pyruvate (Fig. 3F) (58). Similar levels of PDHα1 and intermediate levels of pPDHα1 were seen in Δ(90)+YAP^{S127A}+L30P/R34P tumors. Most notable were pPDHα1 levels in Δ(90)+L30P/R34P tumors and in YAP^{S127A}+L30P/R34P tumors. In the latter case, PDH inactivation was equivalent to that of Δ(90)+L30P/R34P tumors (*SI Appendix* Fig. S5).

Regardless of Δ(90) and YAP^{S127A} status, L30P/R34P tumors expressed more Glut1/Slc2a1 glucose transporter than Δ(90)+YAP^{S127A} tumors (Fig. 3J). In contrast, the higher utilization of pyruvate and overall greater mitochondrial activity of Δ(90)+L30P/R34P tumors was accompanied by increased expression of liver-type phosphofructokinase (PFK-L), glycolysis' rate-limiting enzyme. This suggested that, in addition to higher rates of Oxphos (Fig. 3C-H), these tumors were also engaged in higher levels of glycolysis despite their slower growth rates. Collectively, these findings indicated that pyruvate production and its utilization were under complex but cooperative control by factors that coordinated glucose uptake, its glycolytic flux and its conversion to AcCoA.

The complex relationship between Oxphos and its substrates was underscored in the case of glutaminolysis, which was reduced in most tumor groups relative to liver but up-regulated in Δ(90)+L30P/R34P tumors (Fig. 3G). Yet, levels of mitochondrial glutamate dehydrogenase 1 (Gludh1), which catalyzes glutamate's conversion to α-ketoglutarate, were unchanged and those of mitochondrial glutaminase 1 (Gls1), which catalyzes the rate-limiting conversion of glutamine to glutamate, were actually reduced (Fig. 3J). On the other hand, glutamine synthase, which catalyzes the conversion of cytoplasmic glutamate to glutamine were higher, suggesting that inratumoral glutamine availability might pose a barrier to more extensive glutaminolysis. The extremely low levels of Gludh1 in YAP^{S127A}+L30P/R34P tumors, which might limit the availability of glutamate-derived α-ketoglutarate, may have been offset by a parallel loss of pyruvate carboxylase (PC), which anaplerotically furnishes oxaloacetate from pyruvate. As already demonstrated, the expected increase in pyruvate availability was not associated with greater pyruvate utilization by mitochondria. Instead, the pyruvate might now prove a more abundant source of α-ketoglutarate via alanine transaminase. Finally, in keeping with its reliability as a replication marker (59), proliferating cell nuclear antigen (PCNA) levels closely matched tumor growth rates and survival (Figs. 1A&3A).

RNAseq reveals a key common transformation-specific core of transcripts. That any two members of the Δ(90)+YAP^{S127A}+L30P/R34P trio were oncogenic (Figs. 1A&3A) suggested a model of tumorigenesis (and perhaps cystogenesis), involving a commonly regulated subset of target genes. RNAseq was therefore performed to identify these. Initial principal component analysis (PCA) and hierarchical clustering showed that all tumor cohorts were distinguishable from liver (Fig. 4A and B). Among the former, Δ(90)+YAP^{S127A}+L30P and Δ(90)+YAP^{S127A}+R34P tumors differed in the expression of only a single transcript and were thus combined in subsequent analyses. All other tumor groups were readily distinguishable (Fig. 4B and C). Δ(90)+YAP^{S127A} tumors and Δ(90)+YAP^{S127A}+WT-NFE2L2 tumors differed in the expression of 821 genes (Fig. 4C&D), indicating that WT-NFE2L2 was not entirely silent as suspected from its nuclear localization and its modest buffering of oxidative stress (Fig. 2B and J). In contrast, L30P/R34P tumors showed more transcriptional dysregulation with Δ(90)+YAP^{S127A}+L30P/R34P tumors differing from Δ(90)+YAP^{S127A} and Δ(90)+YAP^{S127A}+WT-NFE2L2 tumors in the expression of 3584 transcripts and 1654 transcripts, respectively (Fig. 4D).

We categorized the 821 gene expression differences between the Δ(90)+YAP^{S127A} and Δ(90)+YAP^{S127A}+WT-NFE2L2 cohorts using Ingenuity Pathway Analysis (IPA). Among the four IPA pathways with the most disparate z-scores (z>+2.8), only one ("NRF2-mediated oxidative stress response"), could be categorized as being NFE2L2-responsive (*SI Appendix* Table S1). In contrast, of the 3584 differences between the Δ(90)+YAP^{S127A} and Δ(90)+YAP^{S127A}+L30P/R34P cohorts, 12 pathways were similarly dysregulated, with three involving redox homeostasis. Finally, comparison of the 1654 differences between the Δ(90)+YAP^{S127A}+WT-NFE2L2 and Δ(90)+YAP^{S127A}+L30P/R34P cohorts showed up-regulation of the "NRF2-mediated oxidative stress response" and "glutathione redox reactions I" pathways in the latter cohort with lower but still significant z-scores. Collectively, these findings indicated that L30P/R34P dysregulated more NFE2L2 target genes.

ChIP-seq results from human HepG2 HB cells in the ENCODE data base (https://www.encodeproject.org/data-standards/chip-seq/) indicated that 4.7-5.5% of the transcripts shown in Fig. 4D were murine orthologs of NFE2L2 direct target genes. The inclusion of data from three additional human cell lines (A549, HeLa-S3 and IMR90) increased these values to 13.8-22.2%. IPA profiling identified additional, variably deregulated pathways among the tumor cohorts with the most prominent one pertaining to Oxphos, mitochondrial dysfunction, cholesterol and bile acid synthesis and cell signaling (Fig. 4E).

41 core transcripts (the "BYN" subset) were deregulated in all tumors irrespective of the primary drivers,

with 29 always being deregulated in the same direction (Fig. 4F). 22 were similarly deregulated in HBs driven by several other patient-derived β-catenin mutants and in slowly-growing Δ(90)+YAP^{S127A} HBs arising in *myc-/-*, *chrebp-/-* and *myc-/-+chrebp-/-* hepatocytes (Table 1) (7, 8). Δ(90)+YAP^{S127A}+L30P/R34P HBs also showed a more pronounced dysregulation of all 22 transcripts than was seen in HBs generated by any of the pair-wise combination of factors. 14 of these transcripts were also dysregulated in Δ(90)+YAP^{S127A}+WT-NFE2L2 tumors, suggesting that, while possibly contributing to tumorigenesis, they were less likely to be involved in the unique growth-accelerating and cystogenic properties of L30P/R34P. Together, these considerations indicated that the remaining eight coordinately de-regulated transcripts contributed to L30P/R34P's cooperation with Δ(90) or YAP^{S127A}. On average, these eight transcripts were deregulated by 47.5 fold in the Δ(90)+YAP^{S127A}+L30P/R34P cohort versus 13-fold in the next highest expressing cohort ($P<0.001$).

A previous analysis of 25 HBs by RNAseq and an earlier microarray-based study of 24 tumors had identified four-member and 16-member unrelated transcript subsets, respectively, whose expression correlated with differential survival (60, 61). In the former case, the favorable survival group was designated as "C1" and the poor and intermediate survival groups were designated "C2A" and "C2B", respectively. Ten of the transcripts listed in Table 1 were differentially expressed by the C1 and C2A/C2B groups (range 2.6-fold up-regulated-8.5-fold down-regulated, $q<0.05$). Hierarchical clustering of the HBs from ref. (61) with these ten transcripts perfectly segregated the C1 and C2A/C2B groups (Fig. 4G). None of the transcripts in Table 1 were included in the previously described gene panels (60, 61).

We next queried all tumors in The Cancer Genome Atlas (TCGA) and, for 17 of the above 22 transcripts, found correlations with survival in 14 cancer types (*SI Appendix* Fig. S6). Recurrent associations were seen in several cancers including the three most common subtypes of kidney cancer and HCC. Some transcripts (ex. gas1, gars and serpin E1) also correlated with survival in multiple cancers. Of the 45 instances in which a gene's expression was associated with a survival difference, the direction of change relative to that of matched normal tissues was discordant in only one case (Gas1) and partially discordant in two others (Rock2 and Uap1l1) (Table 1).

The Cancer Hallmarks Analytics Tool (http://chat.lionproject.net/) was next used to determine the association of the above 22 transcripts with the 10 cancer-promoting/enabling hallmarks proposed by Hanahan and Weinberg (62). 16 transcripts (73%) were associated with one or more hallmarks and eight were associated with five-nine (Table 2). The most common ones included "promotion of genomic instability", "promotion of angiogenesis" and "enhanced proliferative signaling" (10-12 transcripts each). By comparison, five well-known oncogenes and tumor suppressors, with broad roles in diverse human cancers, were individually associated with five-eight hallmarks. Together, these studies show that BYN transcript expression levels frequently correlate with the properties, behaviors and lethality of multiple human cancers, including HBs.

Both the BYN murine gene promoters and their human orthologs contain multiple putative Tcf/Lef, TEAD and ARE binding sites for β-catenin, YAP/TAZ and NFE2L2 respectively (*SI Appendix* Fig. S7). Querying the ENCODE v.5 CHIP-seq data base for sites actually bound by these factors in the HepG2 HB cell line identified considerably fewer of these elements (*SI Appendix* Fig. S8A). 16 BYN genes contained TEAD sites, three contained Tcf/Lef sites and none contained AREs. A more comprehensive survey with Chip-seq data from eight additional human cell lines expanded these numbers to 13 genes with Tcf/Lef sites and two genes with ARE sites. Four more sites were found in previously identified TEAD site-containing genes (*SI Appendix* Fig. S8B). Thus, many of the 22 genes shown in Table 1 are either indirect targets for the above transcription factors or harbor biding sites elsewhere in their promoters.

The *serpine1* gene promoter contained the largest number of functional binding sites for all three transcription factors (*SI Appendix* Fig. S8). Serpin E1 levels were particularly high in Δ(90)+YAP^{S127A}+ L30P/R34P tumors (Fig. 4H), which agreed with RNAseq results (Table 1). Cyst fluid and, to a lesser extent, plasma from tumor-bearing mice also contained readily detectable serpin E1 whereas plasma from mice bearing Δ(90)+YAP^{S127A} tumors contained low-undetectable levels (Fig. 4I).

We next co-expressed a serpin E1-encoding SB vector with Δ(90)+YAP^{S127A}. The median survival of mice bearing the resultant tumors was similar to that of those bearing Δ(90) and YAP^{S127A} tumors (Fig. 1A) (4, 7, 8, 44, 46). Grossly and histologically, these tumors did not contain cysts but did show evidence of extensive necrosis (Fig. 4J and K). Healthy tumor tissue also expressed high levels of exogenous serpin E1 that could

be readily distinguished from endogenous serpin E1 due to the former bearing a Myc epitope tag (Fig. 4L). These results indicated that serpin E1 deregulation could recapitulate one feature of mutant NFE2L2 over-expression, namely extensive necrosis, but was unable to accelerate growth or promote cyst formation.

***NFE2L2* mutations, copy number variations (CNVs) and over-expression in HB and other cancers.** Attesting to the rarity of *NFE2L2* mutations in human HBs, our previous RNA-seq analyses of 45 murine tumors generated by nine different β-catenin variants identified only L30P which was previously described in human tumors and used in the current study (7). We therefore queried RNA-seq or exome-seq data from 257 previously reported primary HBs and cell lines (https://cancer.sanger.ac.uk/cosmic and refs.12, 13, 61, 63) and identified nine NFE2L2 missense mutations (frequency= 3.5%) all of which clustered within or adjacent to the DLG or ETGE domains (*SI Appendix* Table S2). This was lower than the 9.5% incidence of *NFE2L2* gene mutations in HCCs from The Cancer Genome Atlas (TCGA) (31/326, $p<10^{-4}$ using Fisher's exact test, not shown).

In contrast to missense mutations, WT-NFE2L2 over-expression in association with CNVs occurs in as many as half of HBs and involves amplification of the entirety of chromosome 2 or a sub-chromosomal region of chromosome 2 containing the *NFE2L2* locus (12, 13). We quantified *NFE2L2* gene copy numbers in a collection of 22 primary HBs archived at our institution and identified three (13.6%) with 4.0-6.4-fold increases in copy number (*SI Appendix* Fig. S9A). *NFE2L2* amplification was also found at frequencies as high as 20% across numerous other human cancers (https://www.mycancergenome.org/content/gene/nfe2l2/ (*SI Appendix* Fig. S9B).

We obtained *NFE2L2* and *KEAP1* gene expression levels from the TCGA PANCAN data set and compared these with survival in the cancers from *SI Appendix* Fig. S9B that were most prone to *NFE2L2* gene amplification. For each tumor type, NFE2L2 and KEAP transcript levels were divided into four quartiles containing approximately equal numbers of tumors. In HCCs only, tumors with the lowest levels of each transcript were associated with longer survival relative to the group expressing the highest levels (*SI Appendix* Fig. S9C and D).

Transcript and protein levels often correlate poorly, particularly in cancer (64) and this is especially true for NFE2L2 whose activation occurs post-translationally (18, 19, 53, 65). Thus, evaluating survival based solely on transcript levels (*SI Appendix* Fig. S9C and D) might fail to capture NFE2L2's importance in some cancers. A more meaningful way to identify NFE2L2 deregulation that actually reflects the protein's redox-dependency might be to survey tumors for changes in the expression of NFE2L2 direct target gene transcripts. We did this for 46 such targets from the Ingenuity Pathway Analysis Knowledge Base (*SI Appendix* Table S3) in three cancer types from TCGA (head and neck cancer, hepatocellular carcinoma and lung adenocarcinomas). Preliminary analysis indicated these as having the highest likelihood of aberrant NFE2L2 behavior based on transcript up-regulation, gene copy number variation or mutation. Sufficient numbers of normal control tissues were also available for comparison. NFE2L2 transcript expression in these tumors was similar to that in matched normal tissues and did not correlate with the levels of the 46 NFE2L2 target transcripts. As a group however, the latter were significantly up-regulated (1.36-1.63-fold, $P=6.0\times10^{-4}$-6.4×10^{-15}) (Fig. 5A-C) and the survival of individuals whose tumors expressed the highest levels of these target genes was significantly shorter (Fig. 5D-F). This supports the idea that NFE2L2 target gene products suppress ROS and other electrophiles that might otherwise compromise tumor growth and/or spread (18, 23, 52, 53, 65).

Discussion

We have shown here that patient-derived NFE2L2 mutants, but not WT-NFE2L2, markedly accelerate murine liver tumorigenesis, thus supporting the idea that dysregulation of the NFE2L2-KEAP1 axis suppresses oxidative, electrophilic and metabolic stresses and their consequences (1, 3, 6, 14, 15, 24, 25, 28, 65). Depending however on the context and timing, this suppression may have opposite outcomes (14, 16, 17). Early in tumor evolution, it may protect against DNA damage, reduce the accumulation of oncogenic lesions and actually slow tumor initiation or progression (14, 65). At later times this same property might increase the ability to tolerate ROS-generating oncoproteins and contribute to the evolution, survival, expansion and therapy resistance of transformed clones (16, 52, 65, 66). Non-canonical functions of NFE2L2

targets that might also contribute to these features include the regulation of anti- and pro-apoptotic proteins such as Bcl-2 and Bcl-x_L, the reprogramming of metabolism, the regulation of angiogenesis and the detoxification of chemotherapeutics (26, 36, 37, 66). Prior support for these functions, however, has derived largely from *in vitro* studies or from the employment of poorly-characterized and/or molecularly heterogeneous tumor xenografts (14, 66-69). Our findings show that NFE2L2 mutants not only accelerate *de novo* HB tumorigenesis mediated by mutant β-catenin+YAP^{S127A} but are also directly transforming when co-expressed with either of these oncoproteins. This suggests that some HBs may be NFE2L2-driven when only one component of the β-catenin/Hippo axis is de-regulated as occurs frequently (3, 4, 6) Further examination of other cancers harboring *NFE2L2* mutations or CNVs may reveal additional and heretofore unappreciated co-dependencies with other oncoproteins or tumor suppressors. The non-canonical consequences of NFE2L2 activation may perhaps now be understood better in light of this newly described direct oncogenic function.

A unique feature of β-catenin+YAP^{S127A}+L30P/R34P HBs was the presence of numerous fluid-filled cysts (Fig. 1B-E,G and *SI Appendix* Figs. S2-4) (47-49). Tumor vasculature may sometimes arise from actual tumor cells ("pseudovasculature") or tumor-derived endothelium originating from an epithelial to mesenchymal transition (70, 71). However, the large, bloodless structures we observed do not appear to be of a vascular nature. A rare condition known as "peliosis hepatis" is associated with comparably-sized cyst-like lesions that may contain either epithelium or endothelium. However, these too are typically blood-filled and less abundant (72, 73). The cysts we observed appear more akin to those seen occasionally in human HBs (43), appeared unrelated to tumor growth rates and arose only in the context of β-catenin+YAP^{S127A}+mutant NFE2L2 co-expression.

In contrast to its cytoplasmic location in cultured cells, WT-NFE2L2's near-complete nuclear localization *in vivo* (Fig. 2B) was initially puzzling(18, 19, 28, 52, 65). This may perhaps reflect the highly oxidized cytoplasm of tumor cells and/or the elevated levels of dietary electrophiles within hepatocytes (54, 72, 73). Together, these chronic stresses are likely to maintain KEAP1 in a largely oxidized state with any residual activity being responsible for the lower levels of endogenous and exogenously-expressed WT-NFE2L2 (Fig. 2A). The >800 transcript differences between β-catenin+YAP^{S127A}+WT-NFE2L2 tumors and β-catenin+YAP^{S127A} tumors (Fig. 4D) is testimony to the transcriptional consequences of even small amounts of WT-NFE2L2 localizing to the nucleus and the fine balancing of endogenous NFE2L2 and KEAP1 levels. Nevertheless, at the amounts expressed here, WT-NFE2l2 afforded less protection against oxidative stress and was unable to promote tumorigenesis (Figs. 1A and 2J). This also readily explains why either mutations or CNVs of either NFE2L2 or KEAP1 increase the fractional nuclear concentration of NFE2L2 with similar consequences (15, 28, 65, 68).

β-catenin+YAP^{S127A}+L30P/R34P tumors displayed metabolic signatures quite similar to those induced by β-catenin+YAP^{S127A} including lower rates of Oxphos and reduced mitochondrial mass compared to livers (Figs. 2C-I and 3C-I) (7, 8, 46). In contrast, tumors maintained high mitochondrial pyruvate utilization, with variably increased Glut1/Slc2a1, PFK-L and pPDHα1 (Fig. 3F and J). We have suggested that increased activity of PDH, which links glycolysis and Oxphos, allows tumors to compensate for lower β-FAO rates by maximizing the conversion of limiting amounts of pyruvate to AcCoA in the face of ongoing Warburg-type respiration (7, 8, 46, 56). Further efficiency of AcCoA generation might derive from reduced PC, which anaplerotically converts pyruvate to oxaloacetate. This dynamic PDH behavior underscores the balance between β-FAO and glycolysis known as the Randle cycle (74, 75). Its preservation in tumors provides the potential for non-catabolized fatty acids to be redirected into new membrane generation, thus minimizing the need for energy-demanding *de novo* synthesis from more primitive anabolic precursors. Nonetheless, this latter pathway remains intact via the above-described changes in PDH and PC and potentially serves as an alternate source of lipid.

Despite alterations of glutaminolysis pathway enzymes (Fig. 3J), Δ(90)+YAP^{S127A}+L30P/R34P tumors decreased glutamine-driven Oxphos, which is used by some tumors to anaplerotically support α-ketoglutarate pools (74). Collectively, these studies indicate that the metabolic demands of these tumors were largely served via reprogramming of glycolysis and the classical TCA cycle.

In contrast to the afore-mentioned tumors or those reported previously (7, 8, 46), Δ(90)+L30P/R34P HBs were unique in their down-regulation of Glut1/Slc2a1 and up-regulation of PFK-L, a rate-limiting glycolytic enzyme (75). This suggested that lesser amounts of glucose-6-phosphate, PFK-L's immediate upstream

substrate, would be available to supply the pentose phosphate pathway and that less mitochondrial pyruvate might ultimately be needed due to the slower growth rates of these tumors. However, the increased mitochondrial DNA content and Oxphos of these tumors exceeded even that of normal livers by as much as two-three-fold (Fig. 3C-E,I). This enhanced mitochondrial function was evident from the greatly increased responses to all tested substrates, particularly glutamate and palmitoyl-CoA (Fig. 3C-H). Together, these findings underscored a reduced reliance on Warburg-type respiration and a return to a somewhat more liver-like Oxphos profile with its greater dependency on β-FAO as its primary energy source.

In further contrast to the above tumors, the metabolic behavior of YAP^{S127A}+L30P/R34P tumors more closely resembled that of Δ(90)+YAP^{S127A} tumors (Fig. 3C-H) although with different expression patterns of the above proteins. Among the most notable of these differences was the virtual absence of PC. As mentioned above, this could increase the efficiency of pyruvate's conversion to AcCoA.

The generation of tumors with pair-wise combinations of Δ(90), YAP^{S127A} and L30P/R34P and the characterization of their ensuing properties allowed us to assign distinct, albeit general, functional roles to each factor and to identify key individual transcriptional repertoires, which has not previously been possible. Thus, Δ(90), but not YAP^{S127A}, appears to promote a much more metabolically active state by up-regulating both mitochondrial mass and oxidative metabolism in response to all tested substrates. Indeed the related metabolic behaviors of Δ(90)+YAP^{S127A} tumors and YAP^{S127A}+L30P/R34P tumors (Fig. 3C-H) suggest that YAP^{S127A} was dominant over Δ(90) and might even suppress these mitochondrial responses.

Unbiased RNAseq permitted the correlation of specific transcripts with each transcription factor, both individually and in combination (Fig. 4B-F). Importantly, this identified a common core set of 22 transcripts deemed most likely to explain certain key features of Δ(90)+YAP^{S127A}+L30P/R34P tumors, namely their vastly accelerated growth rate, cyst formation and widespread necrosis (Table 1). Further evaluation provided additional reasons to believe in the importance of these transcripts to HBs and other cancers. First, they were all altered in the same direction in response to each possible combination of β-catenin, YAP^{S127A} and L30P/R34P (Table 1 and Fig. 4F). Second, they were expressed in tumors with widely disparate growth rates generated by different β-catenin mutants as well as in growth-impaired tumors (7, 8). Third, all were more deregulated in Δ(90)+YAP^{S127A}+L30P/R34P tumors (Table 1). Fourth, ten of the transcripts perfectly identified human HB groups with favorable and unfavorable outcomes and were distinct from other gene signatures previously used to distinguish these cohorts (Fig. 4G) (60, 61). Lastly, 16 of the 22 transcripts (73%) possessed cancer-promoting or enabling functions (Table 2) (62).

Among the most intriguing of the above 22 transcripts was that encoding serpin E1, a serine protease inhibitor, also known as plasminogen activator inhibitor-1, with important roles in tumor growth, metastasis, angiogenesis and extracellular matrix remodeling in addition to its canonical function in fibrinolysis (76). Serpin E1 transcripts were the second most highly up-regulated in β-catenin+YAP^{S127A}+L30P/R34P tumors (Table 1) and the *serpine1* promoter was unique in containing multiple response elements for each transcription factor (*SI Appendix* Figs. S7 and S8). We also confirmed and extended previous observations that serpin E1 levels correlate with unfavorable survival in numerous human cancers (*SI Appendix* Fig. S6) (77, 78). High levels of circulating serpin E1 and polymorphisms in the human gene's promoter that increase basal expression are associated with polycystic ovary syndrome (PCOS) and the enforced expression of serpin E1 in the murine ovary is sufficient to generate cysts (79-81). While serpin E1 co-expression in β-catenin+YAP^{S127A} HBs did not accelerate their growth rates, or promote cyst formation, the tumors did develop the areas of necrosis that tended to be associated with cysts in β-catenin+YAP^{S127A}+L30P/R34P HBs (Figs. 1D and 4J and K). Thus, while serpin E1 over-expression could impart levels of necrosis equivalent to or higher than those associated with β-catenin+YAP^{S127A}+L30P/R34P tumors, it seems likely that other factors are necessary to recapitulate the rapid growth and cyst formation.

Collectively, our findings demonstrate that NFE2L2 mutants alter intracellular redox balance in β-catenin+YAP^{S127A} HBs, vastly accelerate tumor growth rates and are associated with pronounced cystogenesis and tumor necrosis. The unanticipated oncogenicity of NFE2L2 mutants when co-expressed with either β-catenin or YAP^{S127A} also demonstrated their more direct role in transformation *in vivo* and unequivocally establish NFE2L2 as an oncoprotein. This finding provided an opportunity to identify key transcripts that likely mediate these unique features and that directly contribute to tumorigenesis. The high frequency with which disruption of the NFE2L2-KEAP1 axis occurs in cancer and its prognostic implications can now be better understood in light of these findings.

Materials and Methods

Plasmid DNAs. Plasmids used included Sleeping Beauty (SB) vectors encoding human β-catenin mutants Δ(90) and R582W, yes-associated protein YAP^{S127A}, WT-NFE2L2, $NFE2L2^{L30P}$ (L30P), $NFE2L2^{R34P}$ (R34P), cyto-roGFP mit-roGFP or Myc-epitope-tagged murine Serpin E1 (10 μg each). All plasmids were purified with Plasmid Plus Midi columns using the buffers and instructions provided by the supplier (Qiagen, Inc., Germantown, MD) and were administered to 6–8-week-old FVB mice via HDTVI (7, 8). All inoculate also contained 2 μg of a non-SB vector encoding SB Transposase under the control of a CMV immediate early promoter (7, 8).

Tumor induction in mice. All animal studies were performed in accordance with the Public Health Service Policy on Humane Care and Use of Laboratory Animals Institute for Laboratory Animal Research (ILAR) Guide for Care and Use of Laboratory Animals. They were also approved by the Institutional Animal Care and Use Committee (IACUC) at the University of Pittsburgh. Animals were euthanized when tumors achieved maximally permissible size or at the recommendation of a veterinarian if tumors caused obvious distress. At the time of sacrifice, fresh tissues were used immediately for the indicated metabolic studies or were apportioned into small pieces, snap-frozen in liquid nitrogen, and immediately stored at −80C for future processing.

Oxphos measurements. Respirometry was performed as described previously (45, 46, 55). For this, approx. 50 mg of fresh tissue was disrupted on ice in MiR05 buffer (110 mmol/L sucrose; 3 mmol/L $MgCl_2$; 0.5 mmol/L EGTA; 60 mmol/L potassium lactobionate; 20 mmol/L taurine; 10 mmol/L KH_2PO_4; 20 mmol/L HEPES, pH 7.2; and 1 mg/mL fatty acid-free BSA) and 300 μg of the resulting lysate was used to determine oxygen consumption rates (OCRs) with an Oroboros Oxygraph 2k instrument (Oroboros Instruments, Inc., Innsbruck, Austria). Reactions were performed following the addition of cytochrome c (10 μM), malate (2 mM), pyruvate (5 mM), ADP (5 mM) and glutamate (10 mM) to initiate electron transport chain activity via Complex I. Succinate was then added to a final concentration of 10 mM to allow the sum of Complexes I + II activities to be measured. Upon reaching equilibrium, rotenone (0.5 μM final concentration) was added to inhibit Complex I and to allow the individual contributions of Complex I + Complex II to be confirmed. All activities were then normalized to total protein. To measure mitochondrial β-FAO, palmitoyl-CoA and L-carnitine at final concentrations of 3 μM and 10 μM, respectively were added to reactions already primed with ADP, malate and succinate. Similar studies, performed only in response to L-carnitine alone were used to assess the endogenous stores of potentially oxidizable fatty acids.

Response of tumor cells to oxidative stress. Subsets of mice were injected with the usual SB vectors and additional ones encoding cyto-roGFP or mito-roGFP, which are redox-sensitive forms of GFP that localize to the cytoplasm or mitochondrial matrix respectively (57). At sacrifice, fragments of fresh tumor were finely minced in D-MEM+10% FBS and single cells were allowed to attach to the bottom of a 100 cm tissue culture plate for several days until achieving approx. 80% confluency. The cells were then trypsinized, re-seeded into 6 well-glass bottom tissue culture plates (MatTek, Corp., Ashland, MA) and allowed to attach for 2-3 days. Cells were then visualized in real time in a temperature- and CO_2-controlled environment using a LSM710 laser scanning confocal microscope (Carl Zeiss, Munich, Germany). The ratio of emission signal intensities at 488/405 nm from regions of comparable brightness was used to determine the baseline redox state of each subcellular compartment (57). Cells were then exposed to 5 mM H_2O_2 for 5 min followed by rapid replacement with fresh H_2O_2-free medium. Continuous monitoring was maintained over the next ~40 min to allow the rates at which the cells normalized their redox state to be determined.

TaqMan Assays. To identify CNVs in human HBs, DNAs from stored, de-identified FFPE specimens of eight normal tissues and 22 HBs were isolated using a QIAmp DNA FFPE Tissue Kit, according to the directions of the supplier (Qiagen). Each DNA sample (10 ng) was amplified in triplicate 12 μl reactions using a KAPA Probe Fast qPCR Kit (2x) (GeneWorks, Thebarton, Australia). Each PCR primer's final concentration was 250 nM and each TaqMan probe concentration was 300 nM. The sequences of the NFE2L2 primers were:

(Fwd): 5'-TCATCTACAAACGGGAATGTCT-3', (Rev): 5'-GTTGCCCACATTCCCAAATC-3', TaqMan probe: 5'-56-FAM/AGATGCTTT/ZEN/GTACTTTGAT-3'. Two nuclear genes were used for controls, namely glyceraldehyde-3-phosphate dehydrogenase (GAPDH) and Ribonuclease P RNA Component H1 (RPPH1). The sequences of GAPDH primers were: (Fwd): 5'-CCTAGGGCTCACATATTC-3', (Rev): 5'-CGCCCAATACGACCAAATCTA-3', TaqMan probe: 5'-/5Cy5/TCCTCATGC/TAO/CTTCTTGCCTCTTGT /3IABRQSP/3'. The sequences of RPPH1 PCR primers were: (Fwd): 5'-TCTGGCCCTAGTCTCAGACCTT-'3 , (Rev): 5'-GAGCTGAGTGCGTCCTGTC-3', TaqMan probe: 5'-56-FAM/CCAAGGGAC/ZEN/ATGGGAGTG-3'. Conditions used for target amplification were 95 °C for 10 s followed by 40 cycles at 95 °C for 15 s. and 60 °C for 60 s.

Mitochondrial DNA (mtDNA) content was quantified as previously described (7, 8) using a TaqMan-based approach that amplified a 90 bp segment of the mtD-loop region. The results were normalized to a control TaqMan reaction that amplified a 73 bp region of the nuclear apolipoprotein B gene. Reactions contained 10 ng of total DNA and were performed on a CFX96 Touch™ real-time PCR detection system (Bio-Rad, Inc., Hercules, CA) using the following conditions: 95 °C for 10 s, 40 cycles at 95 °C for 15 s. followed by 60 °C for 60 s.

Immuno-blotting. Tissue lysates were prepared in SDS-lysis buffer containing protease, kinase and phosphatase inhibitors as previously described (7, 8, 46). Immunoblots were developed using SuperSignal™ West Pico Chemiluminescent Substrate kit (Thermo Fisher, Waltham, MA). Antibodies, the vendors from which they were obtained and the conditions used are listed in *SI Appendix* Table S4.

For subcellular fractionation studies, tumors or livers were harvested, sectioned into small fragments, snap-frozen in liquid nitrogen and stored at -80 C. Nuclear and cytoplasmic fractionations were performed on ~100 mg fragments of fresh tissues using a Subcellular Protein Fractionation Kit according to the directions of the supplier (Thermo-Fisher) and as previously described (7).

RNA-seq analysis. RNA purification was performed as previously described using Qiagen RNAeasy columns (7). RIN values were determined with an Agilent 2100 Bioanalyzer (Agilent Technologies, Foster City, CA) and only those >8.5 were used. Samples were prepared for paired-end sequencing using an NEB NEBNext Ultra Directional RNA Library Prep kit (New England Biolab, Beverly, MA) and sequencing was performed on a NovaSeq 600 Instrument (Illumina, Inc., San Diego, CA) by Novagene, Inc. (Sacramento, CA). Raw and processed original data are accessible through GEO (accession number: GSE157623) (https://www.ncbi.nlm.nih.gov/geo/query/acc.cgi?acc= GSE157623). Differentially-expressed transcripts were identified using three different approaches, namely DeSEq2, CLC Genomic Workbench v. 12.0 (Qiagen), and EdgeR and were analyzed using the Galaxy platform (https://galaxyproject.org/use/). For DeSeq2 and EdgeR, FASTQ file reads were mapped against the GRCm38.p6 mouse reference genome using STAR (https://github.com/alexdobin/STAR/releases) version 2.5.2. The output files were analyzed by featureCounts (http://bioinf.wehi.edu.au/featureCounts/) to quantify transcript abundance. Only transcripts whose differential was demonstrated by all three methods are reported and only after significance was adjusted for false discovery using the Bonferonni–Hochberg correction ($q<0.05$). Ingenuity Pathway Analysis (IPA, Qiagen) was used to aid in pathway identification. The following parameters were recorded for each pathway: *p* value, ratios of dysregulated transcripts to all transcripts associated with that pathway (ratio), and predicted pathway activation, inhibition and indeterminate (*Z*-score).

Target gene promoter analysis. Human and mouse genomes were accessed through the BSgenome.Hsapiens.UCSC.hg38 and BSgenome.Mmusculus.UCSC.mm10 R packages, respectively. Gene position information was accessed for human and mouse respectively using the TxDb.Hsapiens.UCSC. hg38.knownGene and TxDb.Mmusculus.UCSC.mm10.knownGene packages respectively. The flank function was used to query the upstream 5000 bp promoter regions for each gene and the searchSeq function of the TFBSTools R package was used to assess the binding sites in these flanking regions using the aforementioned position frequency matrices. Binding position frequency matrices were queried in R from the JASPAR database using the package JASPAR2018 and converted to position weight matrices using the toPWM function of the TFBSTools R package. Sites with a binding score of above 90% were accepted as putative binding sites.

For the analysis of ENCODE information, Chip-Seq Data were accessed from the ENCODE v.5 database

((https://www.encodeproject.org/)) for the terminal transcription factors (TF) of the NFE2L2 (ARE sites), Wnt/β-Catenin (Tcf/Lcf sites), and Hippo/Yap (TEAD sites) pathways. Data were only included from cell lines with readily available IDR thresholded peaks identified, and p-values derived from more than one experimental replicate. The cell lines from which data was obtained included HepG2, A549, Hela-S3, IMR90, GM12867, HCT-116, HEK293T, K562 and PANC-1. The RTrackLayer R package was used to process the data and the R packages BSgenome.Hsapiens.UCSC.hg38 and TxDb.Hsapiens.UCSC.hg38.knownGene were used to align the Chip-Seq data to the promoters of the genes of interest. For figures summarizing the binding of more than one TF, the p-value plotted was the maximum of any of the TFs at that base-pair.

Dysregulation of NFE2L2 and its direct target genes in human cancers. RNA-seq data from 141 HB samples (12, 13, 61) were searched for NFE2L2 mutations using CLC Genomics Workbench 11. The data were uploaded and a track from reference CDS annotation of gene *NFE2L2* was generated from the "Homo_sapiens_refseq_GRCh38.p11_o_Genes" track. Amino acid changes within each sample were found using Basic variant detection: "Toolbox>Resequencing Analysis>Functional Consequences>Variant detection>Basic variant detection" followed by "Amino Acid Changes": "Toolbox>Resequencing Analysis>Functional Consequences>Amino Acid Changes". NFE2L2 mutations from 116 human HBs from the COSMIC Database of were identified by performing a search using "Tissue Distribution>Liver>Sub-Histology> Hepatoblastoma". *NFE2L2* gene CNVs across multiple cancers were identified by analyzing TCGA genomic data in Genomic Data Commons (GDC).

NFE2L2 and KEAP1 transcript expression data were downloaded from the TCGA PANCAN dataset as FPKM, converted to TPM, and filtered to contain only data from HCCs. Samples were defined as having high (top 40%) or low (bottom 40%) levels of KEAP1 and NFE2L2, thus allowing data to be independently categorized according to the expression of each tumor's transcripts. Survival analysis for each group was performed using the Survival package in R, displayed as Kaplan-Meier curves and compared pairwise for log-rank p values. This procedure was repeated for OV, LUSC, ESCA, HNSC, SARC and LUAD tumors.

To determine the relationship between NFE2L2 expression and its direct targets, we used IPA to identify 46 promoters that contained established NFE2L2-binding ARE elements. Expression data (TPM) for these genes and NFE2L2 itself were accessed from the GDC TCGA dataset available on the UCSC Xenabrowser (xena.ucsc.edu) from cohorts with the highest levels of NFE2L2 copy number variations (Fig. 5). Natural log-fold up- or down-regulation for each transcript was computed relative to that in matched normal tissues from the same individual. For visualization purposes, the pairwise correlation matrices of differential values were plotted as a heat map for each cohort, first with transcripts in an arbitrary order that was the same across cohorts, and then as hierarchically clustered heat maps. In all cases only significant correlations were expressed in color with any remaining ones being blacked out. The default settings of the R "ComplexHeatmap" package were used for hierarchical clustering. The predominance of positive correlations was assessed using a binomial test.

Statistical analyses. Survival data for patients in TCGA, were analyzed with GraphPad Prism 7 (GraphPad Software, Inc., San Diego, CA). Depending on the tumor type and "BYN" member transcript being analyzed (Fig. 4E), different expression level cut-offs were used to define the intragroup subsets with the highest and lowest levels of expression (e.g., higest vs. lowest 50%, quartile, etc.). Kaplan-Meier survival curves were generated by Log-rank (Mantel-Cox) test. One-way ANOVA was applied for multiple comparisons using Fisher's least significant difference test. Student's 2-tailed t test was used for comparing differences between 2 groups.

References

1. P. Czauderna *et al.*, Hepatoblastoma state of the art: pathology, genetics, risk stratification, and chemotherapy. *Curr Opin Pediatr* **26**, 19-28 (2014).
2. J. Fuchs *et al.*, Pretreatment prognostic factors and treatment results in children with hepatoblastoma: a report from the German Cooperative Pediatric Liver Tumor Study HB 94. *Cancer* **95**, 172-182 (2002).
3. D. Bell, S. Ranganathan, J. Tao, S. P. Monga, Novel Advances in Understanding of Molecular Pathogenesis of Hepatoblastoma: A Wnt/beta-Catenin Perspective. *Gene Expr* **17**, 141-154 (2017).
4. J. Tao *et al.*, Activation of beta-catenin and Yap1 in human hepatoblastoma and induction of hepatocarcinogenesis in mice. *Gastroenterology* **147**, 690-701 (2014).
5. A. Koch *et al.*, Childhood hepatoblastomas frequently carry a mutated degradation targeting box of the beta-catenin gene. *Cancer Res* **59**, 269-273 (1999).
6. C. Armengol, S. Cairo, M. Fabre, M. A. Buendia, Wnt signaling and hepatocarcinogenesis: the hepatoblastoma model. *Int J Biochem Cell Biol* **43**, 265-270 (2011).
7. W. Zhang *et al.*, beta-Catenin mutations as determinants of hepatoblastoma phenotypes in mice. *J Biol Chem* **294**, 17524-17542 (2019).
8. H. Wang *et al.*, Coordinated Activities of Multiple Myc-dependent and Myc-independent Biosynthetic Pathways in Hepatoblastoma. *J Biol Chem* **291**, 26241-26251 (2016).
9. Q. Min *et al.*, beta-Catenin and Yes-Associated Protein 1 Cooperate in Hepatoblastoma Pathogenesis. *Am J Pathol* **189**, 1091-1104 (2019).
10. S. N. Grobner *et al.*, The landscape of genomic alterations across childhood cancers. *Nature* **555**, 321-327 (2018).
11. X. Ma *et al.*, Pan-cancer genome and transcriptome analyses of 1,699 paediatric leukaemias and solid tumours. *Nature* **555**, 371-376 (2018).
12. M. Eichenmuller *et al.*, The genomic landscape of hepatoblastoma and their progenies with HCC-like features. *J Hepatol* **61**, 1312-1320 (2014).
13. P. Sumazin *et al.*, Genomic analysis of hepatoblastoma identifies distinct molecular and prognostic subgroups. *Hepatology* **65**, 104-121 (2017).
14. A. K. Bauer, T. Hill, 3rd, C. M. Alexander, The involvement of NRF2 in lung cancer. *Oxid Med Cell Longev* **2013**, 746432 (2013).
15. M. J. Kerins, A. Ooi, A catalogue of somatic NRF2 gain-of-function mutations in cancer. *Sci Rep* **8**, 12846 (2018).
16. S. Wu, H. Lu, Y. Bai, Nrf2 in cancers: A double-edged sword. *Cancer Med* **8**, 2252-2267 (2019).
17. M. Dodson *et al.*, Modulating NRF2 in Disease: Timing Is Everything. *Annu Rev Pharmacol Toxicol* **59**, 555-575 (2019).
18. A. Kobayashi *et al.*, Oxidative and electrophilic stresses activate Nrf2 through inhibition of ubiquitination activity of Keap1. *Mol Cell Biol* **26**, 221-229 (2006).
19. M. McMahon, N. Thomas, K. Itoh, M. Yamamoto, J. D. Hayes, Dimerization of substrate adaptors can facilitate cullin-mediated ubiquitylation of proteins by a "tethering" mechanism: a two-site interaction model for the Nrf2-Keap1 complex. *J Biol Chem* **281**, 24756-24768 (2006).
20. K. I. Tong *et al.*, Different electrostatic potentials define ETGE and DLG motifs as hinge and latch in oxidative stress response. *Mol Cell Biol* **27**, 7511-7521 (2007).
21. A. T. Dinkova-Kostova, A. Y. Abramov, The emerging role of Nrf2 in mitochondrial function. *Free Radic Biol Med* **88**, 179-188 (2015).
22. A. T. Dinkova-Kostova *et al.*, Direct evidence that sulfhydryl groups of Keap1 are the sensors regulating induction of phase 2 enzymes that protect against carcinogens and oxidants. *Proc Natl Acad Sci U S A* **99**, 11908-11913 (2002).
23. M. Rojo de la Vega, E. Chapman, D. D. Zhang, NRF2 and the Hallmarks of Cancer. *Cancer Cell* **34**,

21-43 (2018).
24. L. M. Solis *et al.*, Nrf2 and Keap1 abnormalities in non-small cell lung carcinoma and association with clinicopathologic features. *Clin Cancer Res* **16**, 3743-3753 (2010).
25. Y. Kitamura *et al.*, Increased susceptibility to hepatocarcinogenicity of Nrf2-deficient mice exposed to 2-amino-3-methylimidazo[4,5-f]quinoline. *Cancer Sci* **98**, 19-24 (2007).
26. M. Ramos-Gomez *et al.*, Sensitivity to carcinogenesis is increased and chemoprotective efficacy of enzyme inducers is lost in nrf2 transcription factor-deficient mice. *Proc Natl Acad Sci U S A* **98**, 3410-3415 (2001).
27. B. N. Chorley *et al.*, Identification of novel NRF2-regulated genes by ChIP-Seq: influence on retinoid X receptor alpha. *Nucleic Acids Res* **40**, 7416-7429 (2012).
28. J. D. Hayes, M. McMahon, NRF2 and KEAP1 mutations: permanent activation of an adaptive response in cancer. *Trends Biochem Sci* **34**, 176-188 (2009).
29. D. Malhotra *et al.*, Global mapping of binding sites for Nrf2 identifies novel targets in cell survival response through ChIP-Seq profiling and network analysis. *Nucleic Acids Res* **38**, 5718-5734 (2010).
30. G. Y. Liou, P. Storz, Reactive oxygen species in cancer. *Free Radic Res* **44**, 479-496 (2010).
31. M. Ogrunc *et al.*, Oncogene-induced reactive oxygen species fuel hyperproliferation and DNA damage response activation. *Cell Death Differ* **21**, 998-1012 (2014).
32. P. T. Schumacker, Reactive oxygen species in cancer cells: live by the sword, die by the sword. *Cancer Cell* **10**, 175-176 (2006).
33. L. Diebold, N. S. Chandel, Mitochondrial ROS regulation of proliferating cells. *Free Radic Biol Med* **100**, 86-93 (2016).
34. D. E. Heppner, A. van der Vliet, Redox-dependent regulation of epidermal growth factor receptor signaling. *Redox Biol* **8**, 24-27 (2016).
35. S. K. Kim *et al.*, Increased expression of Nrf2/ARE-dependent anti-oxidant proteins in tamoxifen-resistant breast cancer cells. *Free Radic Biol Med* **45**, 537-546 (2008).
36. S. K. Niture, A. K. Jaiswal, Nrf2 protein up-regulates antiapoptotic protein Bcl-2 and prevents cellular apoptosis. *J Biol Chem* **287**, 9873-9886 (2012).
37. S. K. Niture, A. K. Jaiswal, Nrf2-induced antiapoptotic Bcl-xL protein enhances cell survival and drug resistance. *Free Radic Biol Med* **57**, 119-131 (2013).
38. A. J. Kowaltowski, R. G. Fenton, G. Fiskum, Bcl-2 family proteins regulate mitochondrial reactive oxygen production and protect against oxidative stress. *Free Radic Biol Med* **37**, 1845-1853 (2004).
39. J. M. Dolezal *et al.*, Sequential adaptive changes in a c-Myc-driven model of hepatocellular carcinoma. *J Biol Chem* **292**, 10068-10086 (2017).
40. R. Faraonio *et al.*, p53 suppresses the Nrf2-dependent transcription of antioxidant response genes. *J Biol Chem* **281**, 39776-39784 (2006).
41. S. Chowdhry *et al.*, Loss of Nrf2 markedly exacerbates nonalcoholic steatohepatitis. *Free Radic Biol Med* **48**, 357-371 (2010).
42. K. Le Gal *et al.*, Antioxidants can increase melanoma metastasis in mice. *Sci Transl Med* **7**, 308re308 (2015).
43. L. Lignitto *et al.*, Nrf2 Activation Promotes Lung Cancer Metastasis by Inhibiting the Degradation of Bach1. *Cell* **178**, 316-329 e318 (2019).
44. J. H. Miller, The ultrasonographic appearance of cystic hepatoblastoma. *Radiology* **138**, 141-143 (1981).
45. H. Wang *et al.*, Myc and ChREBP transcription factors cooperatively regulate normal and neoplastic hepatocyte proliferation in mice. *J Biol Chem* **293**, 14740-14757 (2018).
46. L. E. Jackson *et al.*, Genetic Dissociation of Glycolysis and the TCA Cycle Affects Neither Normal nor Neoplastic Proliferation. *Cancer Res* **77**, 5795-5807 (2017).
47. A. S. Bhatt *et al.*, Nonneoplastic Cystic Lesions of the Central Nervous System-Histomorphological Spectrum: A Study of 538 Cases. *J Neurosci Rural Pract* **10**, 494-501 (2019).

48. F. A. Carone, R. Bacallao, Y. S. Kanwar, The pathogenesis of polycystic kidney disease. *Histol Histopathol* **10**, 213-221 (1995).
49. P. Rawla, T. Sunkara, P. Muralidharan, J. P. Raj, An updated review of cystic hepatic lesions. *Clin Exp Hepatol* **5**, 22-29 (2019).
50. M. G. Vander Heiden, L. C. Cantley, C. B. Thompson, Understanding the Warburg effect: the metabolic requirements of cell proliferation. *Science* **324**, 1029-1033 (2009).
51. Q. Qu, F. Zeng, X. Liu, Q. J. Wang, F. Deng, Fatty acid oxidation and carnitine palmitoyltransferase I: emerging therapeutic targets in cancer. *Cell Death Dis* **7**, e2226 (2016).
52. H. Motohashi, M. Yamamoto, Nrf2-Keap1 defines a physiologically important stress response mechanism. *Trends Mol Med* **10**, 549-557 (2004).
53. C. J. Schmidlin, M. B. Dodson, L. Madhavan, D. D. Zhang, Redox regulation by NRF2 in aging and disease. *Free Radic Biol Med* **134**, 702-707 (2019).
54. T. Fiaschi, P. Chiarugi, Oxidative stress, tumor microenvironment, and metabolic reprogramming: a diabolic liaison. *Int J Cell Biol* **2012**, 762825 (2012).
55. X. Gao, B. Schottker, Reduction-oxidation pathways involved in cancer development: a systematic review of literature reviews. *Oncotarget* **8**, 51888-51906 (2017).
56. S. Kulkarni *et al.*, Ribosomopathy-like properties of murine and human cancers. *PLoS One* **12**, e0182705 (2017).
57. G. T. Hanson *et al.*, Investigating mitochondrial redox potential with redox-sensitive green fluorescent protein indicators. *J Biol Chem* **279**, 13044-13053 (2004).
58. E. Saunier, C. Benelli, S. Bortoli, The pyruvate dehydrogenase complex in cancer: An old metabolic gatekeeper regulated by new pathways and pharmacological agents. *Int J Cancer* **138**, 809-817 (2016).
59. R. A. Goodlad, Quantification of epithelial cell proliferation, cell dynamics, and cell kinetics in vivo. *Wiley Interdiscip Rev Dev Biol* **6** (2017).
60. S. Cairo *et al.*, Hepatic stem-like phenotype and interplay of Wnt/beta-catenin and Myc signaling in aggressive childhood liver cancer. *Cancer Cell* **14**, 471-484 (2008).
61. K. B. Hooks *et al.*, New insights into diagnosis and therapeutic options for proliferative hepatoblastoma. *Hepatology* **68**, 89-102 (2018).
62. D. Hanahan, R. A. Weinberg, Hallmarks of cancer: the next generation. *Cell* **144**, 646-674 (2011).
63. L. Valanejad *et al.*, PARP1 activation increases expression of modified tumor suppressors and pathways underlying development of aggressive hepatoblastoma. *Commun Biol* **1**, 67 (2018).
64. Y. Liu, A. Beyer, R. Aebersold, On the Dependency of Cellular Protein Levels on mRNA Abundance. *Cell* **165**, 535-550 (2016).
65. E. Kansanen, S. M. Kuosmanen, H. Leinonen, A. L. Levonen, The Keap1-Nrf2 pathway: Mechanisms of activation and dysregulation in cancer. *Redox Biol* **1**, 45-49 (2013).
66. I. I. C. Chio, D. A. Tuveson, ROS in Cancer: The Burning Question. *Trends Mol Med* **23**, 411-429 (2017).
67. M. Sunamura *et al.*, Heme oxygenase-1 accelerates tumor angiogenesis of human pancreatic cancer. *Angiogenesis* **6**, 15-24 (2003).
68. D. A. Frohlich, M. T. McCabe, R. S. Arnold, M. L. Day, The role of Nrf2 in increased reactive oxygen species and DNA damage in prostate tumorigenesis. *Oncogene* **27**, 4353-4362 (2008).
69. T. Kaur, K. L. Khanduja, R. Gupta, N. M. Gupta, K. Vaiphei, Changes in antioxidant defense status in response to cisplatin and 5-FU in esophageal carcinoma. *Dis Esophagus* **21**, 103-107 (2008).
70. M. J. Hendrix, E. A. Seftor, A. R. Hess, R. E. Seftor, Vasculogenic mimicry and tumour-cell plasticity: lessons from melanoma. *Nat Rev Cancer* **3**, 411-421 (2003).
71. T. F. McGuire, G. B. Sajithlal, J. Lu, R. D. Nicholls, E. V. Prochownik, In vivo evolution of tumor-derived endothelial cells. *PLoS One* **7**, e37138 (2012).
72. J. A. Cook *et al.*, Oxidative stress, redox, and the tumor microenvironment. *Semin Radiat Oncol* **14**, 259-266 (2004).

73. F. Weinberg, N. Ramnath, D. Nagrath, Reactive Oxygen Species in the Tumor Microenvironment: An Overview. *Cancers (Basel)* **11** (2019).
74. E. S. Goetzman, E. V. Prochownik, The Role for Myc in Coordinating Glycolysis, Oxidative Phosphorylation, Glutaminolysis, and Fatty Acid Metabolism in Normal and Neoplastic Tissues. *Front Endocrinol (Lausanne)* **9**, 129 (2018).
75. N. Al Hasawi, M. F. Alkandari, Y. A. Luqmani, Phosphofructokinase: a mediator of glycolytic flux in cancer progression. *Crit Rev Oncol Hematol* **92**, 312-321 (2014).
76. V. R. Placencio, Y. A. DeClerck, Plasminogen Activator Inhibitor-1 in Cancer: Rationale and Insight for Future Therapeutic Testing. *Cancer Res* **75**, 2969-2974 (2015).
77. M. H. Kubala, Y. A. DeClerck, The plasminogen activator inhibitor-1 paradox in cancer: a mechanistic understanding. *Cancer Metastasis Rev* **38**, 483-492 (2019).
78. B. R. Binder, J. Mihaly, The plasminogen activator inhibitor "paradox" in cancer. *Immunol Lett* **118**, 116-124 (2008).
79. J. K. Devin *et al.*, Transgenic overexpression of plasminogen activator inhibitor-1 promotes the development of polycystic ovarian changes in female mice. *J Mol Endocrinol* **39**, 9-16 (2007).
80. E. Diamanti-Kandarakis *et al.*, The prevalence of 4G5G polymorphism of plasminogen activator inhibitor-1 (PAI-1) gene in polycystic ovarian syndrome and its association with plasma PAI-1 levels. *Eur J Endocrinol* **150**, 793-798 (2004).
81. S. Lin, G. Yongmei, Plasminogen activator and plasma activator inhibitor-1 in young women with polycystic ovary syndrome. *Int J Gynaecol Obstet* **100**, 285-286 (2008).

Figures

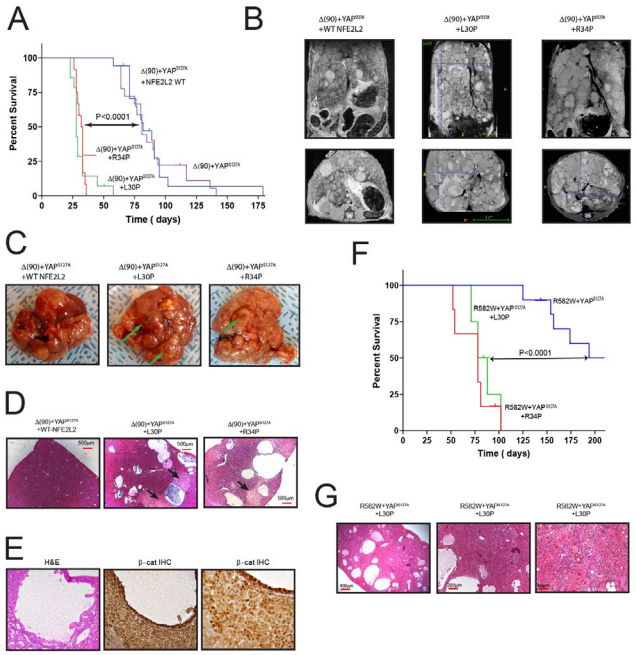

Fig. 1. NFE2L2 mutants L30P and R34P accelerate HB growth. *(A)* Kaplan-Meier survival curves of the indicated cohorts, n=10-12 mice/group. *(B)* MRI images of comparably sized tumors just prior to sacrifice. *(C)* Gross appearance of typical tumors from each of the groups with examples of typical fluid-filled cysts indicated by arrows. *(D)* H&E-stained sections of the tumors shown in *C* showing multiple cysts with areas of prominent adjacent necrosis indicated by arrows. *(E)* Higher power magnification of H&E- and β-catenin IHC-stained sections showing the lumens of cysts lined with cells resembling tumor cells that stain strongly for nuclearly-localized β-catenin. *(F)* Kaplan-Meier survival curves of mice expressing β-catenin missense mutant R582W, YAP^{S127A} and the indicated NFE2L2 proteins. *(G)* H&E stained sections of the indicated tumors from *(F).*

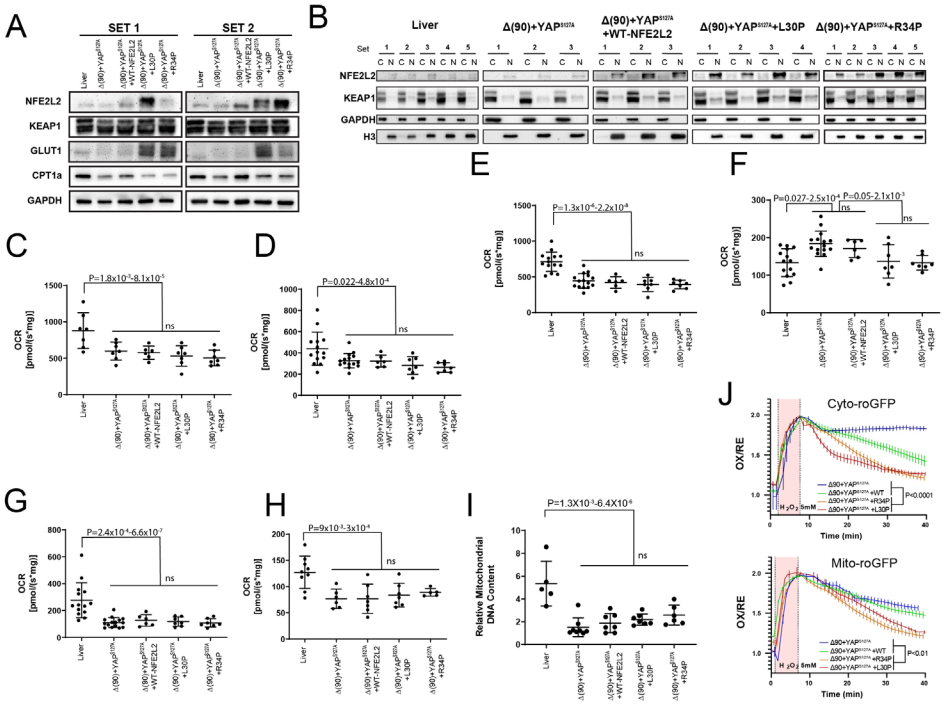

Fig. 2. Distribution and metabolic consequences of L30P/R34P expression in HBs. *(A)* Expression of NFE2L2, KEAP1, GLUT1/Slc2a1 and Cpt1a in two representative sets of total lysates from the indicated tissues. *(B)* Nuclear (N)/cytoplasmic (C) fractionation of the indicated tissues n=3-5 samples/group. GAPDH and histone H3 (H3) immunoblots were performed to control for protein loading and to confirm the purity of each fraction. *(C)* Total OCRs of mitochondria from the indicated tissues in the presence of malate, ADP, pyruvate, glutamate and succinate. *(D)* Complex I responses, calculated following the addition of rotenone to the reactions in (C). *(E)* Complex II responses as determined from residual activity following the addition of Rotenone. *(F)* Responses to pyruvate. *(G)* Responses to glutamate. *(H)* β-FAO responses following the addition of malatae, L-carnitine, and palmitoyl-CoA. *(I)* Quantification of mitochondrial DNA (mtDNA) in representative tissues. TaqMan reactions amplified a segment of the mt D-loop region (8). Each point represents the mean of triplicate TaqMan reactions after normalizing to a control TaqMan reaction for the ApoE nuclear gene. *(J) In vitro* recovery from oxidative stress. Monolayer cultures of the indicated tumor cells expressing cyto-roGFP or mito-roGFP were exposed to 5 mM hydrogen peroxide (bar) while being monitored by live cell confocal microscopy (57).

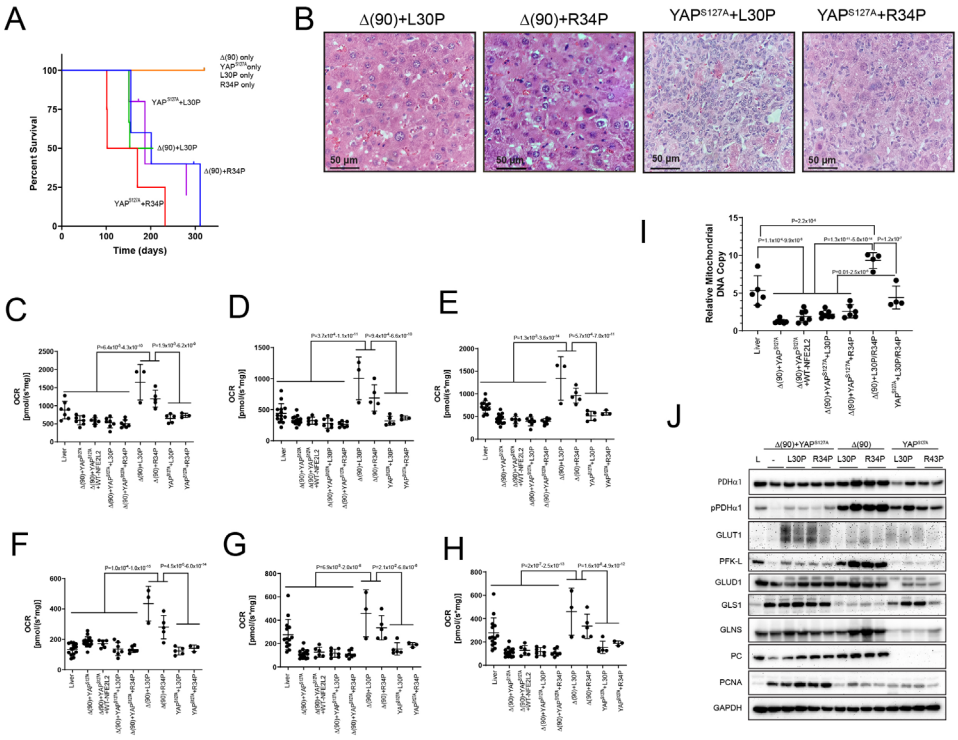

Fig. 3. Characteristics of tumors generated by L30P and R34P co-expressed with Δ(90) or YAP^{S127A}. *(A)* Kaplan-Meier survival curves. Survival was determined as described in Fig. 1A. *(B)* Histopathologic features of representative tumors from the indicated cohorts. See *SI Appendix* Fig. S4 for additional images. *(C-H)* OCRs performed as described in Fig. 2 C-H. *C*=Total Oxphos; *D*=Complex I; *E*=Complex II; *F*=pyruvate response; *G*=glutamate response; *H*= β-FAO. *(I)* mtDNA content of representative tumors from the indicated cohorts performed as described in Fig. 2I. *(J)* Immunoblots from representative tissues of the indicated cohorts. GAPDH was used as a loading control.

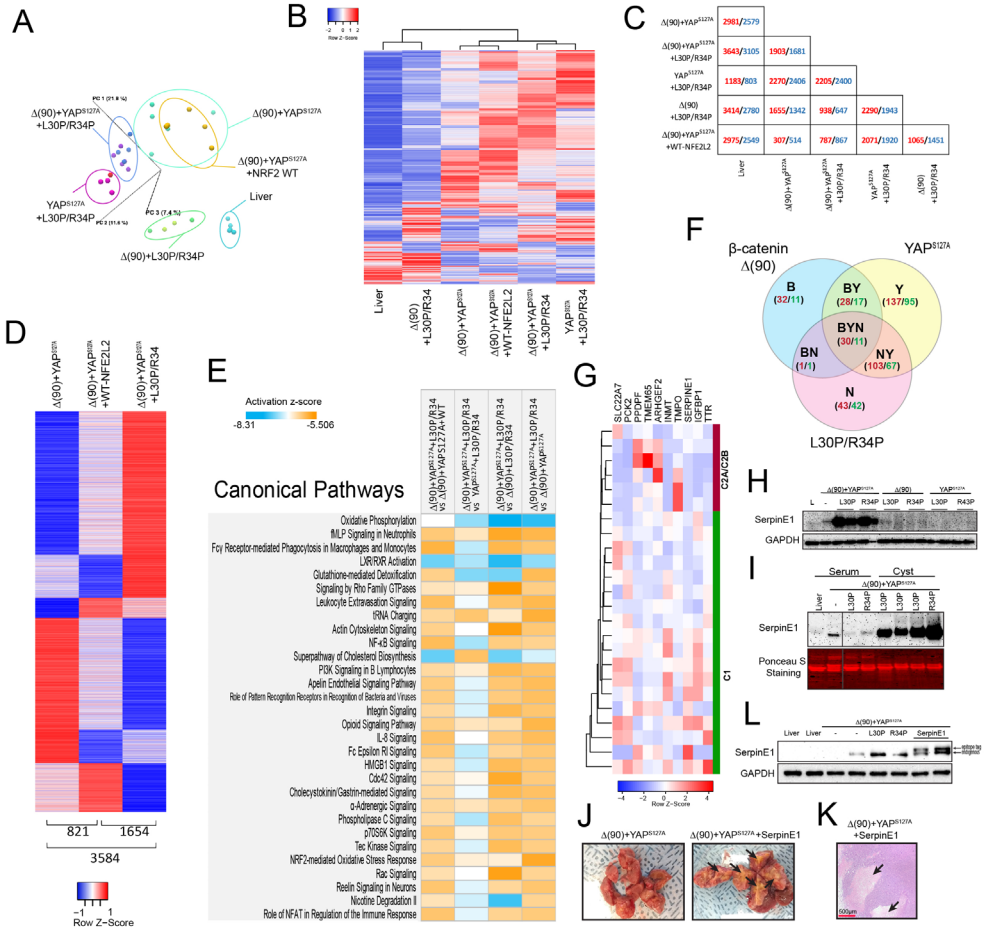

Fig. 4. RNAseq analysis of individual tumor groups generated by combinations of β-catenin, YAP^{S127A}, WT-NFE2L2, L30P and R34P. *(A)* PCA of transcriptomic profiles of livers and tumors (n=4-5 samples/group. *(B)* Heat maps of differentially expressed transcripts from the tissues depicted in *(A)* arranged by hierarchical clustering. Because only a single transcript difference was found between tumors expressing L30P and R34P, results were combined for this and subsequent analyses (L30P/R34P). Red=up-regulated in tumor vs. liver; blue=down-regulated in tumor vs. liver. *(C)* Pairwise comparisons showing the number of significant gene expression differences between any two of the tissues depicted in *(B).* Red and blue=up- and down-regulated, respectively, in the tumors depicted at the left relative to those indicated at the bottom *(D)* Distinct transcript patterns of tumors expressing NFE2L2-WT and L30P/R34P relative to those expressing Δ(90)+YAP^{S127A} only. Numbers indicate the significant expression differences between each pair-wise comparison. *(E)* Top IPA pathways among different tumor groups, expressed as z-scores. Orange=up-regulated; blue=down-regulated. *(F)* Shared gene expression subsets between and among the indicated cohorts. Red and green=number of transcripts up-regulated and down-regulated, respectively, relative to liver. *(G)* Hierarchical clustering of C1 and C2A/C2B subsets (61) of human HBs using the ten "BYN" transcripts from Table 1 that were found to be dysregulated in human tumors. *(H)* Serpin E1 levels in the indicated tissues. *(I)* Serpin E1 levels in plasma and cyst fluid from the indicated cohorts. Plasma and cyst fluids were diluted proportionately and 40 μg of each was subjected to SDS-PAGE. A comparable amount of lysate from one of the Δ(90)+YAP^{S127A}+L30P/R34P tumors depicted in *(I)* was included to allow a comparison among the different samples. In order to take into account differences in the types of samples present, Ponceau acid red staining of the membrane was used to confirm protein concentrations. *(J)* Gross appearance of Δ(90)+YAP^{S127A}+serpin E1 tumors showing extensive necrosis (arrow). *(K)* Histologic appearance of a typical section from the tumor shown in J with peri-cystic necrotic areas indicated by arrows. *(L).* Immunoblots for serpin E1. Note slower mobility of exogenously expressed serpin E1 due to presence of epitope tag.

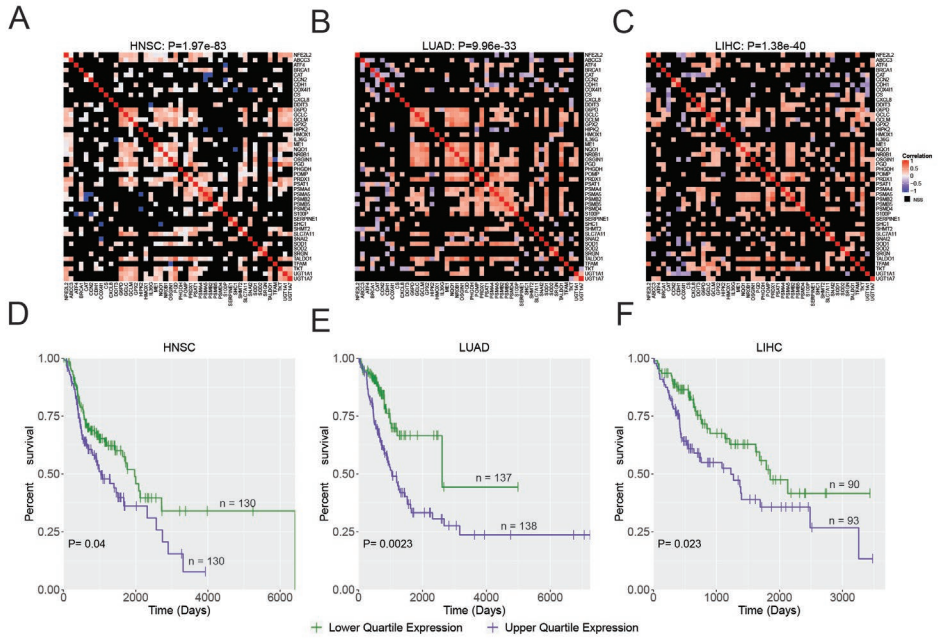

Fig. 5. Correlation between NFE2L2 and its target genes in three human cancer types. *(A-C)* Correlation matrices of NFE2L2 and 46 NFE2L2 target gene transcripts (*SI Appendix* Table S3) from three of the tumor groups depicted in *SI Appendix* Fig. S9B (*A*=head & neck squamous cell cancer [HNSC], *B*=lung adenocarcinoma [LUAD]), *C*=HCC [LIHC]. The preponderance of positive correlations is apparent and was assessed using a binomial test (P values shown at the top of each panel). *(D-F)* Long-term survival of patients whose tumors are profiled in A-C. The levels of expression of the 46 NFE2L2 target genes (*SI Appendix* Table S3) were averaged across all samples for each cancer type. The survival differences between the two quartiles of individuals whose tumors expressed the highest and lowest levels of these transcripts were determined using standard Kaplan-Meier survival and were assessed using log-rank tests.

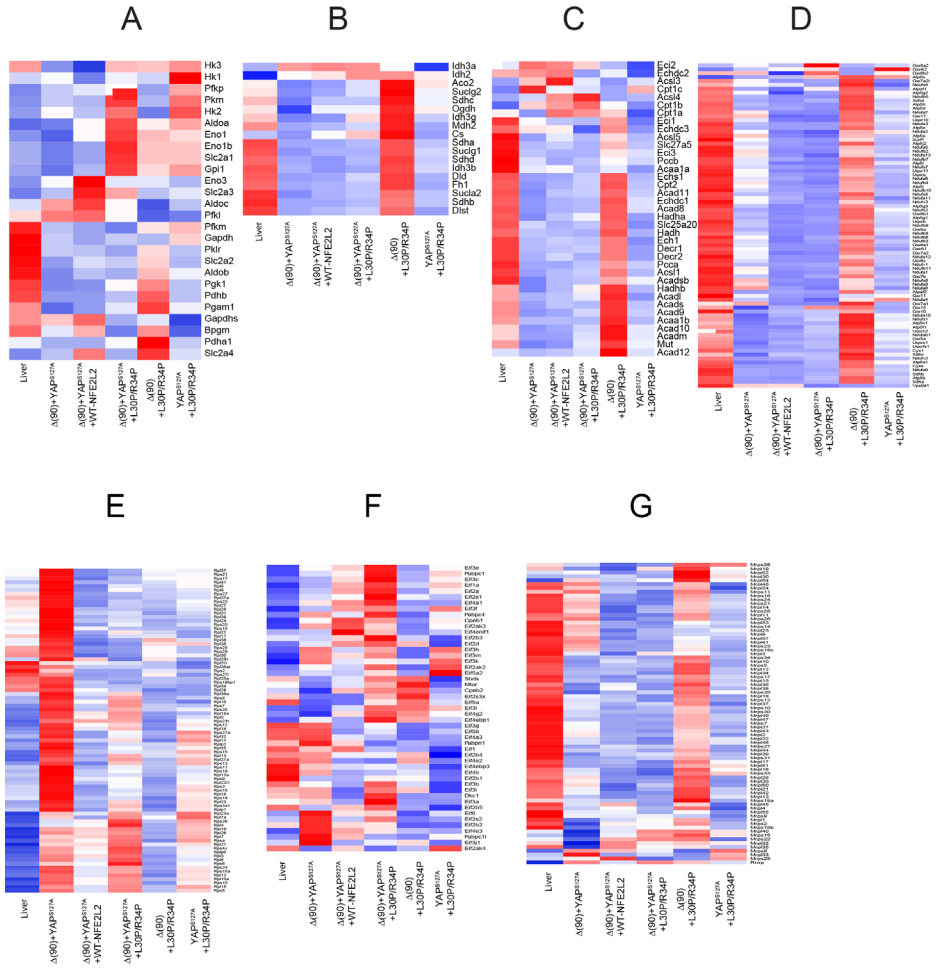

Fig. 6. Differential expression of transcripts involved in metabolism and ribosomal biogenesis and function. Tissues from each of the indicated cohorts (n=5/group) were subjected to RNAseq and analyzed for differential expression of the indicated transcripts. *(A)* Glycolysis pathway, *(B)* TCA Cycle, *(C)* β-FAO, *(D)* Electron transport chain, *(E)* Ribosomal structural proteins. *(F)* Translation elongation factors, *(G)*. mitochondrial ribosomal structural proteins.

Table 1. Gene responsiveness to the indicated combinations of Δ(90), YAP^{S127A} and L30P/R34P

			Expression in HBs Fold change vs Liver				
Name Of gene	Mouse GeneID	Human GeneID	Δ (90)+ YAP^{S127A}	Δ (90)+ L30PR34P	YAP^{S127A}+ L30PR34P	Δ (90)+ YAP^{S127A}+ L30PR34P	Association with shortened survival in human cancers (red=up-regulated; green=down-regulated)$^{+}$
Slc22a7	108114	10864	-25.69	-7.41	-13.99	-109.62	KIRC, LIHC
Inmt	21743	11185	-10.55	-5.52	-3.85	-31.22	LIHC
Gas1	14451	2619	-6.98	-3.76	-6.84	-22.76	THCA, KIRC,KIRP,KICH,COAD,READ, STAD
Atp5k*	11958	521	-2.28	-1.89	-5.73	-11.40	
Ttr*	22139	7276	-5.35	-2.71	-3.31	-9.42	
Cmtm8	70031	152189	-2.67	-1.95	-1.98	-6.14	KIRC, KIRP
Ppdpf*	66496	79144	-2.16	-1.89	-2.51	-3.74	KIRP,KICH
Camkk2*	207565	10645	-1.69	-1.66	-1.79	-3.51	
Tmem65*	74868	157378	2.08	1.82	1.99	2.95	UCEC
Tpm1*	22003	7168	2.69	2.05	2.52	3.50	BLCA,
Tgfa*	21802	7039	2.12	2.33	2.62	3.98	PAAD,THCA ,
Tmpo*	21917	7112	2.91	1.67	2.71	4.25	KIRP,KICH
Gars*	353172	2617	2.86	1.68	2.01	4.57	KIRC, KIRP,KICH,BLCA,LIHC,BRCA
Rock2*	19878	9475	2.77	2.83	3.08	5.22	KIRC, KIRP,KICH
Il22ra1*	230828	58985	3.15	3.80	3.40	6.58	
Arhgef2*	16800	9181	4.93	1.86	4.45	8.72	KIRC,KICH,LIHC
Acot9*	56360	23597	8.89	2.39	7.67	13.02	LIHC
Pck2	74551	5106	6.95	2.22	6.22	15.99	LIHC
Lgals3	16854	3958	7.06	2.34	8.42	18.40	
Uap1l1*	227620	91373	15.51	6.65	16.40	23.67	LIHC,PAAD
Serpine1	18787	5054	7.35	9.25	11.86	43.70	KIRC, KIRP,KICH,LIHC,STAD,HNSC
Igfbp1	16006	3484	58.42	12.80	31.41	132.32	KIRC,LUAD, STAD

The 22 transcripts listed here are a subset of the original 41 "BYN" groups depicted in Fig. 4E that remained after eliminating those that were not regulated in the same direction in each case or that were not also deregulated in tumors driven by other types of b-catenin mutations or in tumors arising from *myc-/-* and/or *chrebp-/-* hepatocytes.

*Also deregulated by D90+YAP^{S127A}+WT-NFE2L2 tumors

+See *SI Appendix* Fig. S6 for Kaplan-Meier survival curves.

Table 2. Association of relevant "BYN" transcripts with The Hallmarks of Cancer

	SLC22A7	*GAS1*	*TTR*	*CMTM8*	*CAMKK2*	*TPM1*	*TGFA*	*TMPO*	*GARS1*	*ROCK2*	*ARHGEF2*	*ACOT9*	*PAK2*	*LGALS3*	*SERPIN E1*	*IGFBP1*	*MYCC*	*KRAS*	*TP53*	*RB*	*PIK3CA*
Invasion/metastasis		●		●	●	●	●			●				●	●	●	●	●	●		●
Immune system evasion					●									●							
Deregulated metabolism					●		●			●		●	●			●	●		●		●
Replicative immortalization		●							●								●	●	●	●	●
Evasion of growth inhibition signals		●			●	●		●		●					●		●		●	●	
Promotion of genomic instability	●	●	●		●	●	●	●	●			●	●	●		●	●	●	●	●	●
Promotion of angiogenesis		●	●		●	●	●			●	●			●	●	●	●		●	●	
Resistance to apoptotic stimuli		●		●	●	●	●	●		●				●		●		●	●	●	●
Enhanced proliferative signaling		●		●	●	●	●			●			●	●	●	●	●		●	●	●
Pro-inflammatory state				●	●					●	●			●	●	●		●			

Each gene at the top of the Table was queried in The Cancer Hallmarks Analytics Tool website (http://chat.lionproject.net/) to identify the hallmarks that have been previously associated with the gene's mutation or dysregulation (62). Those shown in red were included as examples of genes that have been broadly implicated in the causation of multiple different mammalian cancers.

Supplementary Materials for

Patient-Derived Mutant Forms of NFE2L2/NRF2 Drive Aggressive Murine Hepatoblastomas

Huabo Wang, Jie Lu, Jordan A. Mandel, Marie Schwalbe, Joanna Gorka, Ying Liu, Brady Marburger, Jinglin Zhang, Sarangarajan Ranganathan, Edward V. Prochownik

Corresponding author:
Edward V. Prochownik, M.D., Ph.D.
Email: procev@chp.edu

This PDF file includes:

Figures S1 to S9
Tables S1 to S4

Supplementary Figures

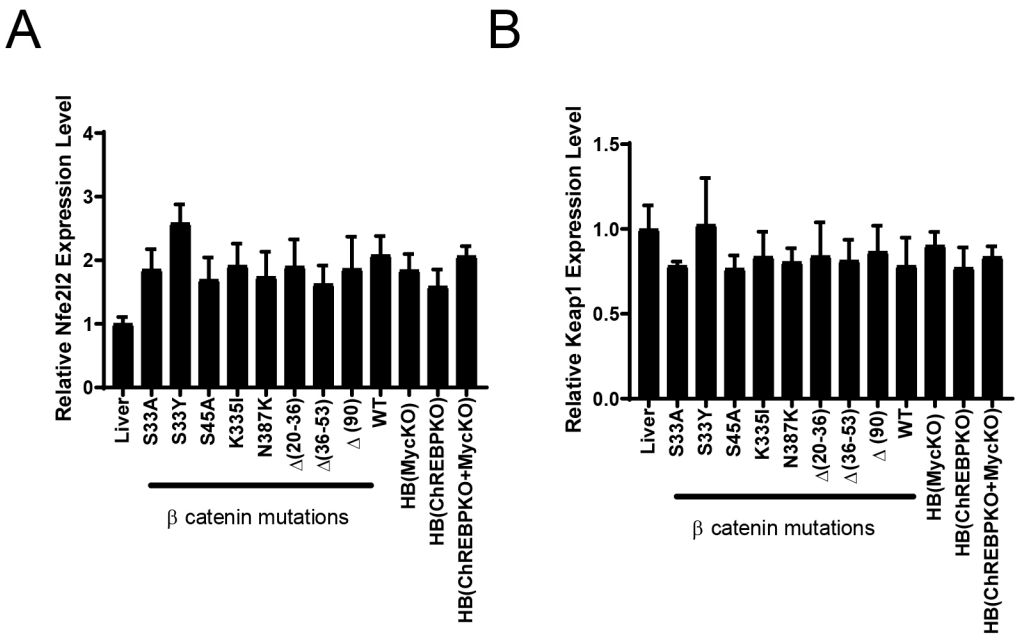

***SI Appendix* Fig. S1.** NFE2L2 and KEAP1 transcript levels in murine HBs and HCCs. *(A)* NFE2L2 transcript levels were quantified from previously reported RNA-seq data obtained from murine HBs that had been generated by the enforced hepatic overexpression of YAP^{S127A} and 8 missense or in-frame deletion mutants of β-catenin or WT β-catenin (7). Transcripts were also quantified in Δ(90) β-catenin-generated HBs arising in *myc-/-, chrebp-/-* and *myc-/-*x*chrebp-/-* hepatocyte backgrounds (8, 45) and in HCCs induced by the conditional over-expression of Myc (56). All transcript levels are expressed relative to those in normal liver (n=5 samples/group). *(B)* KEAP1 transcript levels in the tissues shown in A**.**

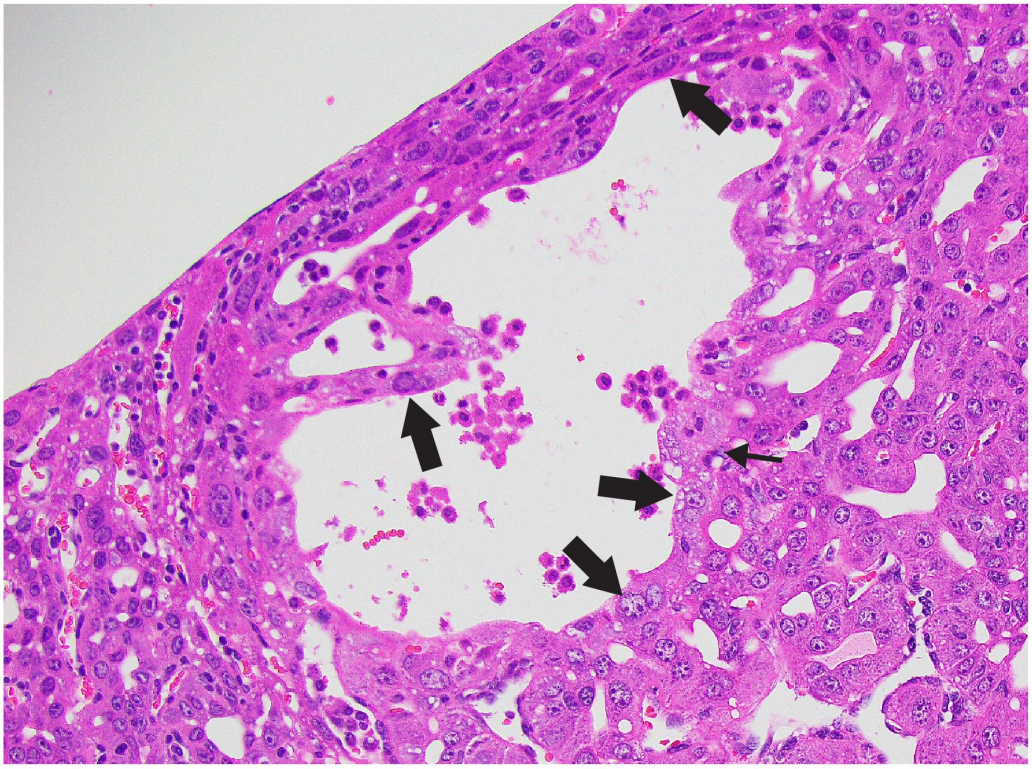

***SI Appendix* Fig. S2.** Cyst structure. High power magnification of an H&E-stained section showing the lumen of a typical cyst in an HB generated by the combination of Δ(90)+YAP^{S127A}+L30P (Fig. 1D). The cyst is lined with cells indistinguishable from those lying deeper in the parenchyma and includes some multiple nucleated typical of hepatocytes (arrows). A presumptive mitotic tumor cell is indicated by the arrowhead.

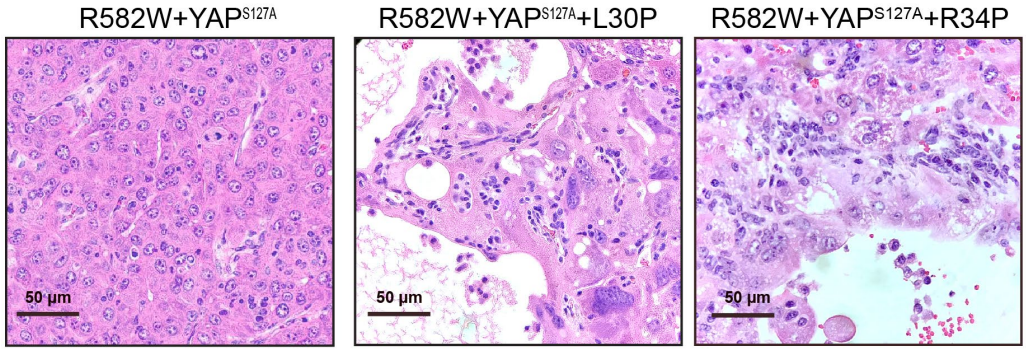

***SI Appendix* Fig. S3.** H&E-stained sections of tumors generated by R582W+YAP^{S127}+/-L30P/R34P. Note that all tumors more closely resemble HCCs than HBs but that those expressing L30P or R34P show more cellular atypia, a greater number of mitoses and extensive cyst formation. See Zhang et al (ref. 7) for additional images of R582W+YAP^{S127} tumors.

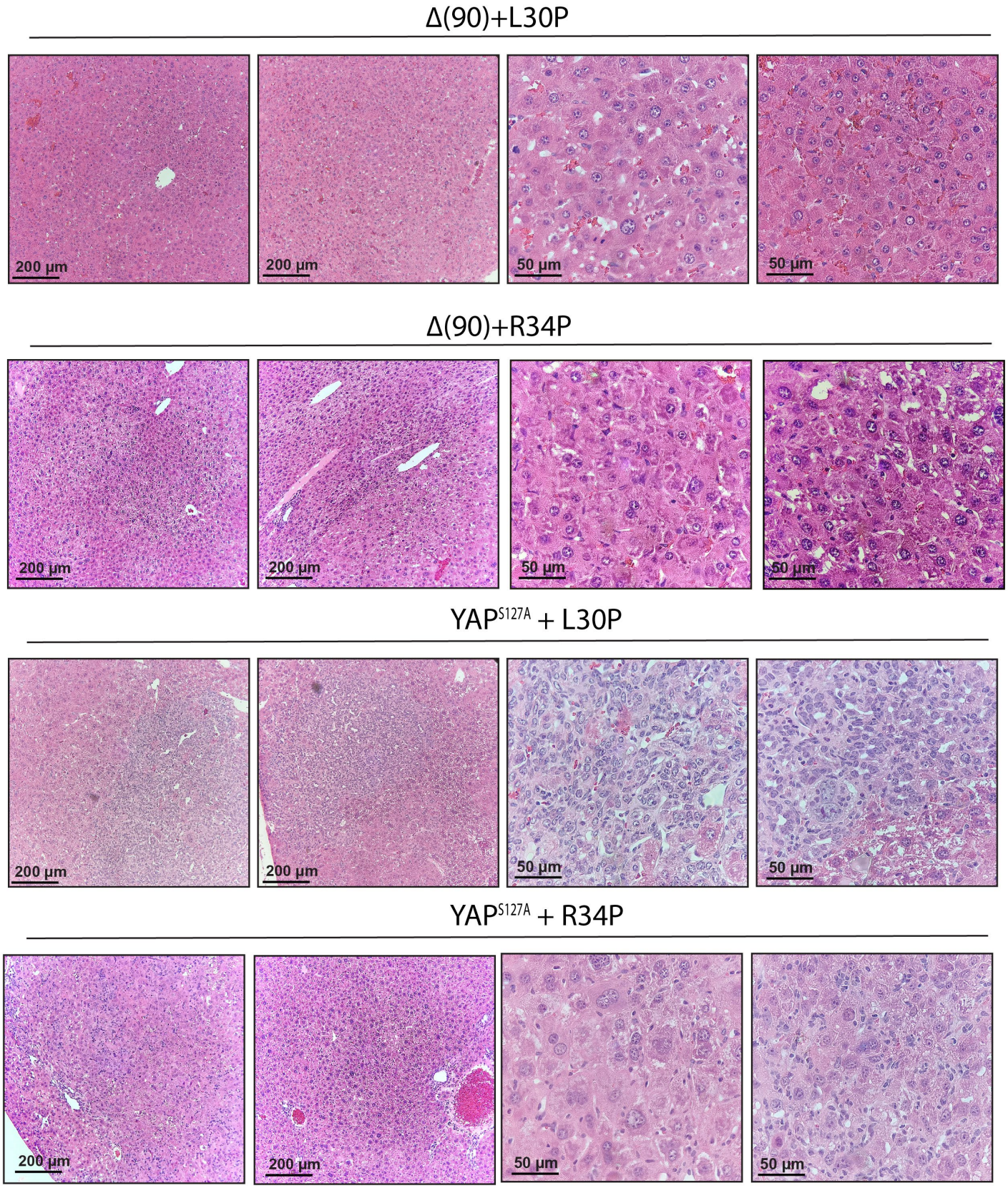

***SI Appendix* Fig. S4.** Additional H&E images of representative tumors.

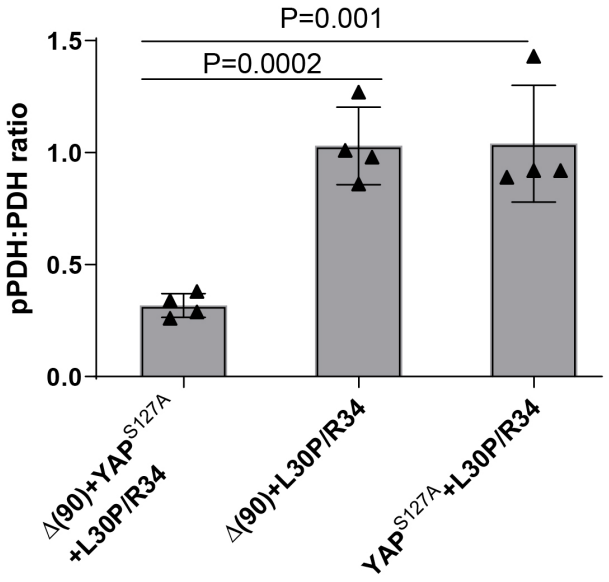

***SI Appendix* Fig. S5.** Quantification of PDH and pPDH immunoblot results from Fig. 3J.

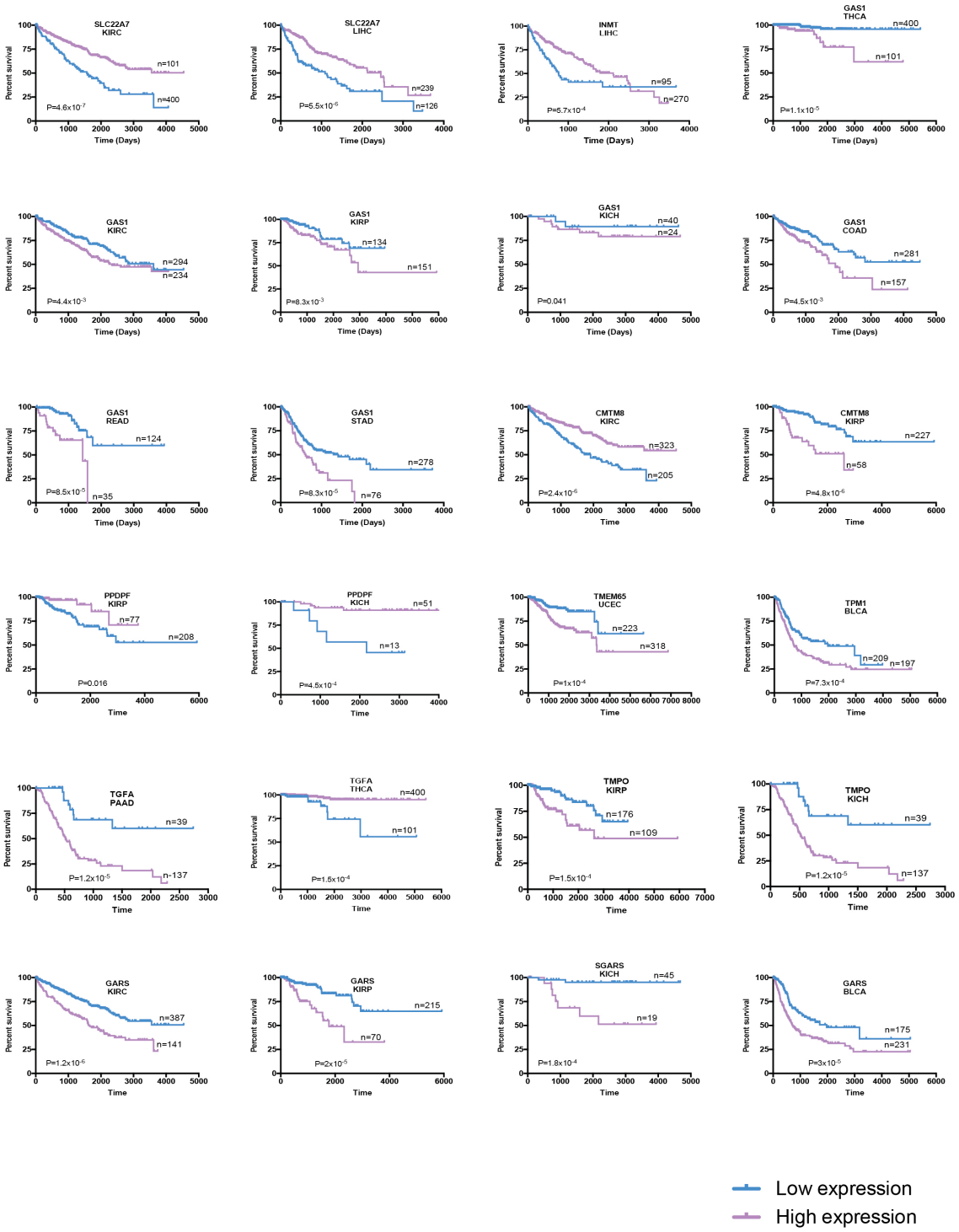

***SI Appendix* Fig. S6.** Correlation between expression levels of transcripts listed in Table 1 and survival in select human cancers. Each depicted tumor type was divided into two groups displaying the highest and lowest expression of the indicated transcript. Standard Kaplan-Meir survival curves for each group were then generated and P values were determined by a standard rank test.

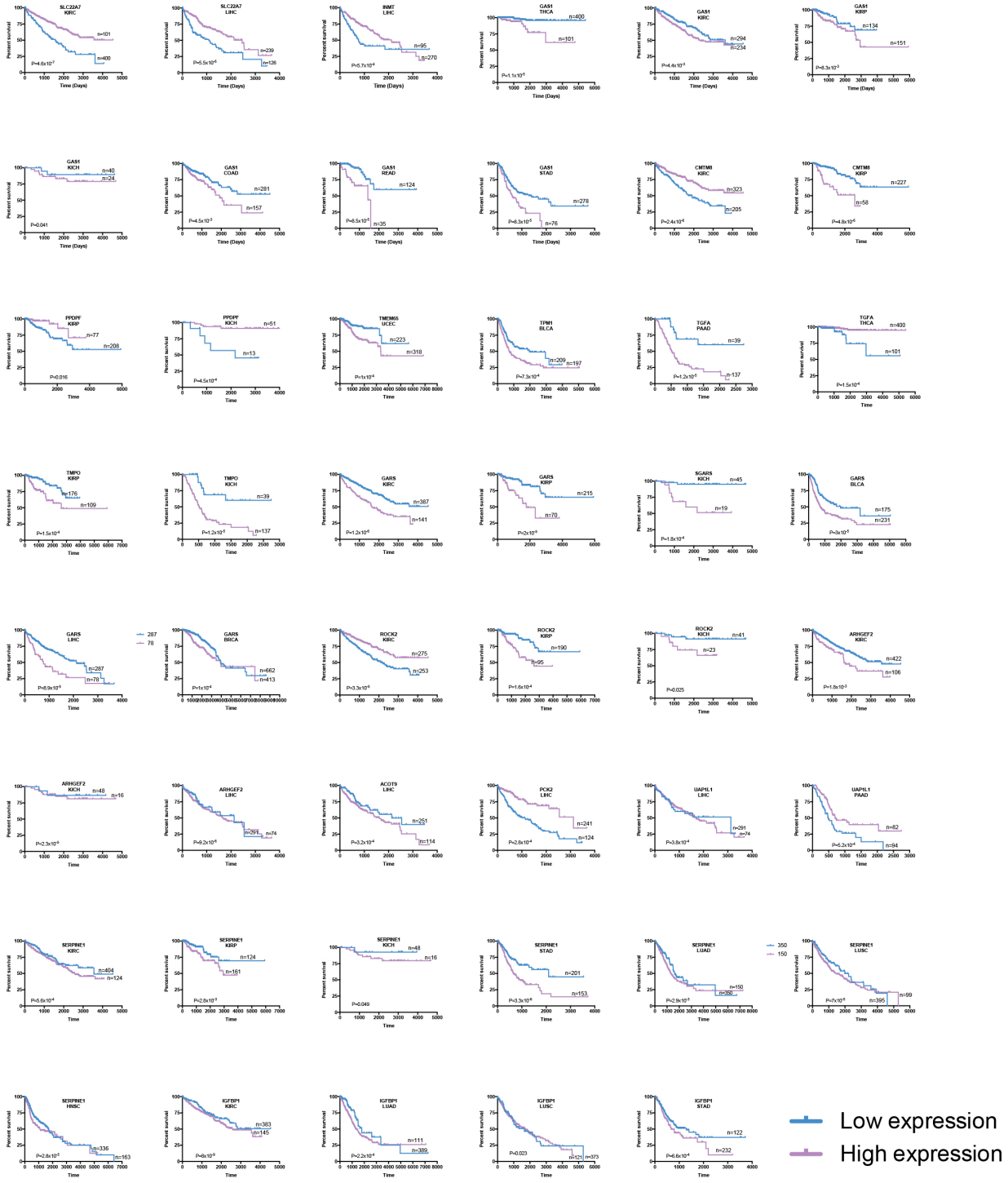

***SI Appendix* Fig. S6 (continue).** Correlation between expression levels of transcripts listed in Table 1 and survival in select human cancers. Each depicted tumor type was divided into two groups displaying the highest and lowest expression of the indicated transcript. Standard Kaplan-Meir survival curves for each group were then generated and P values were determined by a standard rank test.

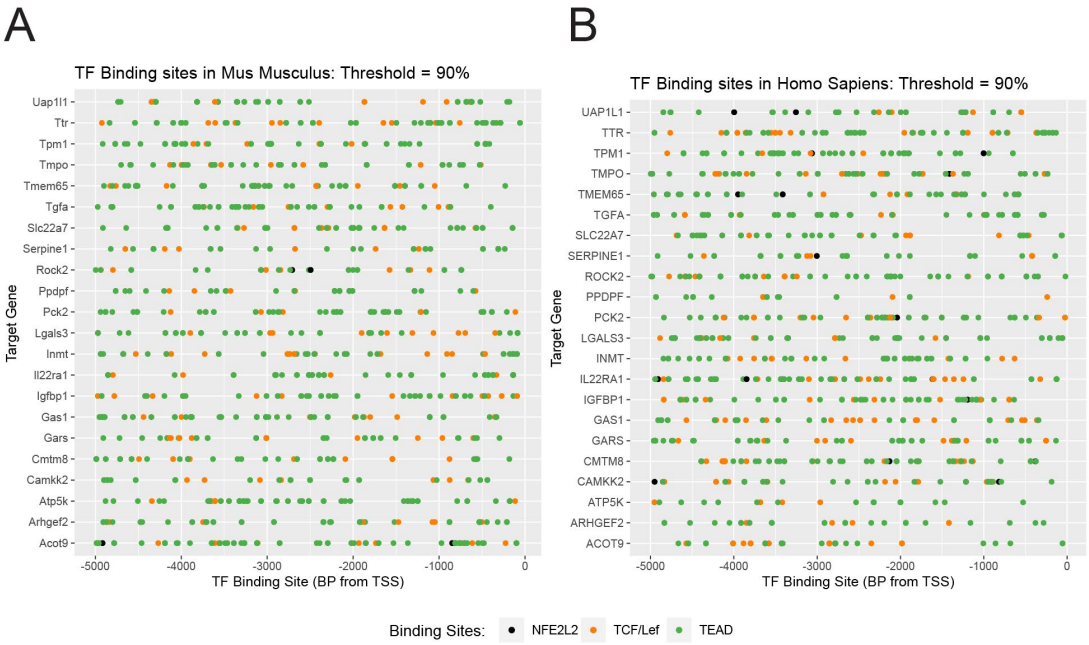

***SI Appendix* Fig. S7.** *In silico* promoter analysis. 5 kb of upstream promoter sequence for each of the murine and human genes listed in Table 1 were screened for the presence of consensus elements for Tcf/Lef, TEAD and ARE binding sites.

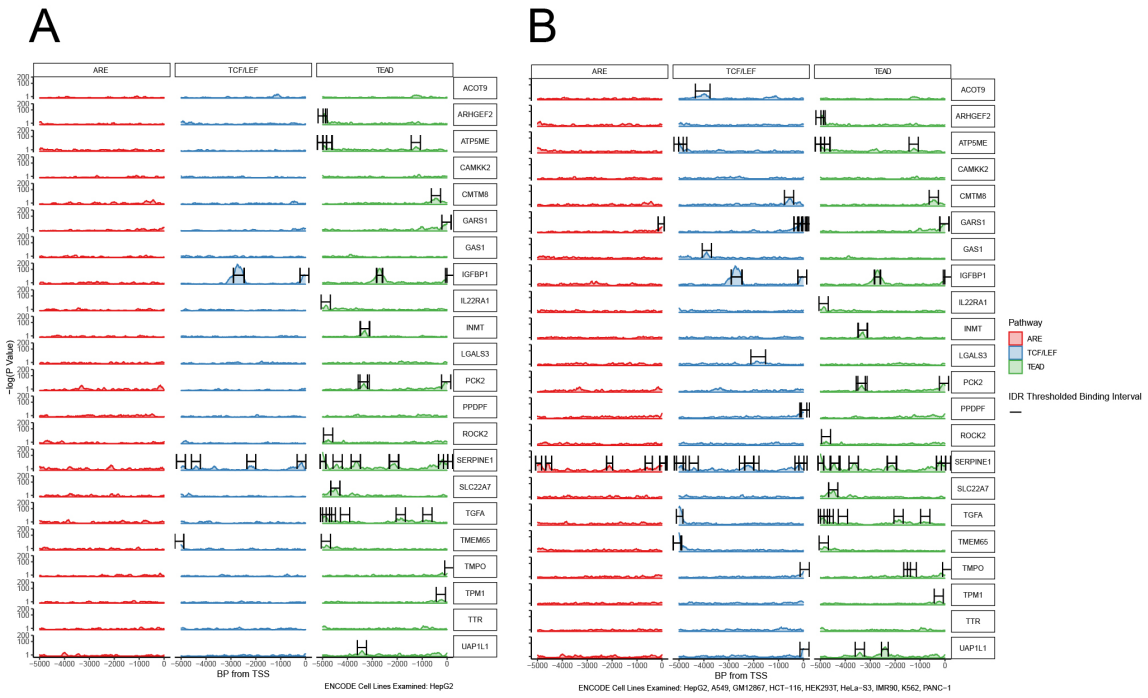

***SI Appendix* Fig. S8.** CHIP-seq results. *(A)* True binding sites for Tcf/Lef, TEAD and ARE obtained from human HepG2 hepatoblastoma cells in the Encode v.5 data base (https://www.encodeproject.org/data-standards/chip-seq/) were mapped to the promoter sequences from *SI Appendix* Fig. S7*(B)* Binding sites for Tcf/Lef, TEAD and ARE following the evaluation of Chip-Deq data from eight other human cell lines (see Materials and Methods).

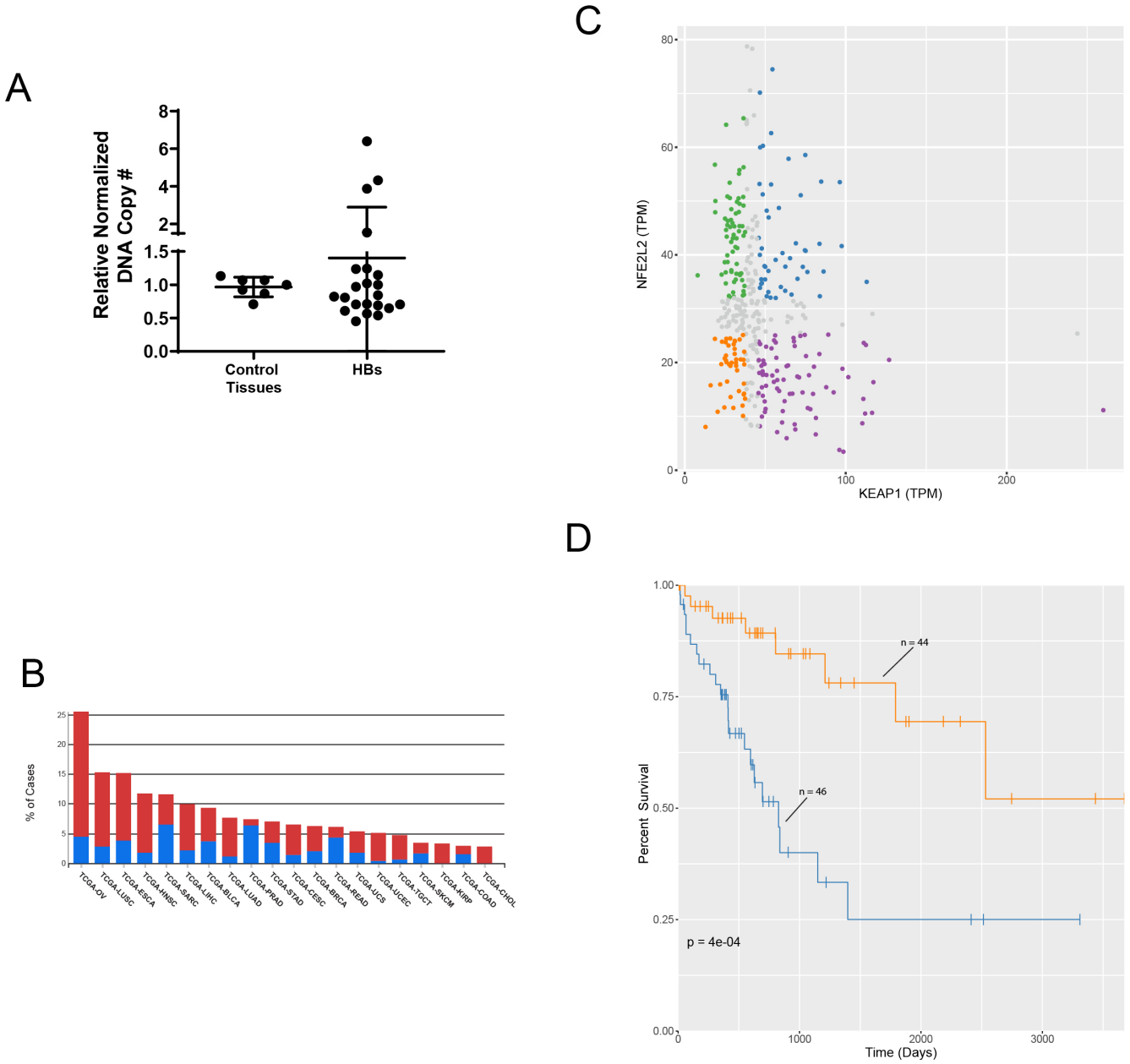

***SI Appendix* Fig. S9.** CNVs in HB and select human tumors. *(A) NFE2L2* CNVs determined from FFPE samples of seven normal tissues and 22 primary HBs. A TaqMan-based assay was used to quantify the copy number ratios of *NFE2L2* versus two control genes (*GAPDH* and *RPPH1*). Each reaction was performed in triplicate and each point represents the calculated mean of the empirically-determined CNVs relative to those of the two control genes. *(B)* Primary human tumors with the highest frequency of *NFE2L2* gene amplification. Data were obtained from the Genomic Data Commons site in TCGA. *(C)* Scatterplots of NFE2L2 and KEAP1 transcript expression in 371 HCC samples from the TCGA PANCAN data set. Sets are divided into quadrants that indicate those samples with the highest and lowest expression of NFE2L2 and KEAP1. *(D)* Kaplan-Meier survival of individuals from C whose tumors contained the highest and lowest levels of *NFE2L2* and *KEAP1* expression.

SI Appendix Table S1 : Top IPA Pathways Deregulated in HBs Expressing WT NFE2L2 vs. L30P/R34P

Name of IPA Pathway	Δ90+YAP^{S127A} +L30P/R34P vs. Δ90+YAP^{S127A} Z-score	Name of IPA Pathway	Δ90+YAP^{S127A} +WT-NFE2L2 vs. Δ90+YAP^{S127A} Z-score	Name of IPA Pathway	Δ90+YAP^{S127A} +L30P/R34P vs. Δ90+YAP^{S127A} +WT-NFE2L2 Z-score
NRF2-mediated Oxidative Stress Response*	3.888	Oxidative Phosphorylation	-4.359	Fcγ Receptor-mediated Phagocytosis in Macrophages and Monocytes	3.71
tRNA Charging	3.771	EIF2 Signaling	-3.128	NF-κB Signaling	3.266
Leukocyte Extravasation Signaling	3.43	Sirtuin Signaling Pathway	2.985	Leukocyte Extravasation Signaling	3.157
Glutathione-mediated Detoxification*	3.317	NRF2-mediated Oxidative Stress Response*	2.828	IL-8 Signaling	3
Role of Pattern Recognition Receptors in Recognition of Bacteria and Viruses	3			Superpathway of Cholesterol Biosynthesis	-3
Ephrin Receptor Signaling	3			Role of NFAT in Regulation of the Immune Response	2.858
RAN Signaling	3			Reelin Signaling in Neurons	2.84
Apelin Endothelial Signaling Pathway	2.985			LXR/RXR Activation	-2.828
Fcγ Receptor-mediated Phagocytosis in Macrophages and Monocytes	2.982			fMLP Signaling in Neutrophils	2.673
Opioid Signaling Pathway	2.92			Fc Epsilon RI Signaling	2.668
fMLP Signaling in Neutrophils	2.828			NRF2-mediated Oxidative Stress Response*	2.558
Glutathione Redox Reactions I*	2.828			Apelin Endothelial Signaling Pathway	2.53
				TREM1 Signaling	2.53
				ERK5 Signaling	2.53
				Role of Pattern Recognition Receptors in Recognition of Bacteria and Viruses	2.496
				NER Pathway	2.449
				Glutathione Redox Reactions I*	2.449

* Red Indicates redox-regulated pathway

***SI Appendix* Table S2: Previously identified *NFE2L2* point mutations in primary human HBs and HB cell lines**

Number of tumors	NFE2L2 mutations identified	Reference
24	None	Hooks et al (61)
34	R34Gx2, D29N	Sumazin et al (13)
47 + 4 cell lines	L30P, R34G, R34P, T80Ax2	Eichenmuller (12)
32	None	Valanejad (63)
116	D77Y	COSMIC

SI Appendix Table S3: 46 NFE2L2 target gene transcripts from IPA

Symbol	Synonym(s)	Entrez Gene Name	Location	Family	Entrez Gene ID		
					Human	Mouse	Rat
ABCC3	1700019L09Rik, ABC31, ATP binding cassette subfamily C member 3, ATP-binding cassette C3, ATP-binding cassette, sub-family C (CFTR/MRP), member 3, cMOAT2, EST90757, MLP2, MOAT-D, MRP3, Multidrug Resistant Protein 3	ATP binding cassette subfamily C member 3	Plasma Membrane	transporter	8714	76408	140668
ATF4	activating transcription factor 4, C/ATF, CREB-2, TAXREB67, TXREB	activating transcription factor 4	Nucleus	transcription regulator	468	11911	79255
BRCA1	BRCA1 DNA repair associated, BRCA1, DNA repair associated, BRCAI, BRCC1, breast cancer 1, early onset, BROVCA1, FANCS, PNCA4, PPP1R53, PSCP, RNF53	BRCA1 DNA repair associated	Nucleus	transcription regulator	672	12189	497672
CAT	2210418N07, ACATALASIA, Cas-1, Cat01, Catalase, Catalase1, Catl, CS1	catalase	Cytoplasm	enzyme	847	12359	24248
CCN2	AMPHIROGULIN, cellular communication network factor 1, cellular communication network factor 2, CTGF, CTGF isoform 1, CTGRP, Fibroblast-inducible secreted, Fisp12, HCS24, IGFBP8, IGFBP-RP2, NOV2, Tissue growth factor	cellular communication network factor 2	Extracellular Space	growth factor	1490	14219	64032
CDH1	AA960649, ARC-1, BCDS1, cadherin 1, Cadherin E, CD324, CDHE, CSEIL, E-cadherin, ECAD, L-CAM, Um, UVO, uvomorulin	cadherin 1	Plasma Membrane	other	999	12550	83502
COX4I1	AL024441, CcO IVi1, COX, COX IV-1, COX4, COX4-1, COX4A, COX4I, COXIV, cytochrome c oxidase subunit 4I1, IV-1	cytochrome c oxidase subunit 4I1	Cytoplasm	enzyme	1327	12857	29445
CS	2610511A05Rik, 9030605P22Rik, AhI4, BB234005, Cis, citrate synthase	citrate synthase	Cytoplasm	enzyme	1431	12974	170587
CXCL8	C-X-C motif chemokine ligand 8, GCP-1, IL8, LECT, LUCT, LYNAP, MDNCF, MONAP, Monocyte-derived neutrophil chemotactic factor, NAF, NAP-1	C-X-C motif chemokine ligand 8	Extracellular Space	cytokine	3576		
DDIT3	AC144852.1, AltDDIT3, C/EBP homology, C/EBP-homologous, C/EBPzeta, Cebp Zeta, Cebp ζ, CEBPZ, CHOP, CHOP-10, DNA DAMAGE-INDUCIBLE transcript, DNA-damage inducible transcript 3, GADD153, RM4	DNA damage inducible transcript 3	Nucleus	transcription regulator	1649	13198	29467
G6PD	G28A, G6PD1, G6PDX, Glucose-6-P Dehydrogenase, glucose-6-phosphate dehydrogenase, glucose-6-phosphate dehydrogenase X-linked, Gpdx	glucose-6-phosphate dehydrogenase	Cytoplasm	enzyme	2539	14381	24377
GCLC	D9Wsu168e, gamma GCS HEAVY CHAIN, Gamma Glutamyl Cysteine Synthetase Light Subunit, Gamma Glutamylcysteine Synthetase, Gamma glutamylcysteine synthetase heavy subunit, GCL, GCS, GCS, Catalytic, GCS-HS, Ggcs-hs, GLCL, GLCL-H, GLCLC, glutamate-cysteine ligase catalytic subunit, Glutamate-Cysteine Ligase, Catalytic Subunit, γ Gcs, γ GCS HEAVY CHAIN, γ Glutamyl Cysteine Synthetase Light Subunit, γ Glutamylcysteine Synthetase, γ glutamylcysteine synthetase heavy subunil γ-Gcsh	glutamate-cysteine ligase catalytic subunit	Cytoplasm	enzyme	2729	14629	25283
GCLM	AI649393, Gamma gclm, gamma GCS LIGHT CHAIN, Gamma glutamylcysteine synthase (regulatory), gamma GLUTAMYLCYSTEINE SYNTHETASE, gamma-glutamylcysteine synthetase light (regulatory) subunit, Gcmc, Gcs, Regulatory, Gcs-ls, GLCLR, glutamat-cystein ligase, regulatory subunit, glutamate-cysteine ligase modifier subunit, Glutamate-Cysteine Ligase, Modifier Subunit, γ gclm, γ GCS LIGHT CHAIN, γ glutamylcysteine synthase (regulatory), γ GLUTAMYLCYSTEINE SYNTHETASE, γ-glutamylcysteine synthetase light (regulatory) subunit	glutamate-cysteine ligase modifier subunit	Cytoplasm	enzyme	2730	14630	29739
GPX2	GI-GPx, glutathione peroxidase 2, GPRP, GPRP-2, GPX-GI, GSHPx-2, GSHPX-GI	glutathione peroxidase 2	Cytoplasm	enzyme	2877	14776	29326
HIPK2	1110014O20RIK, B230339E18RIK, homeodomain interacting protein kinase 2, LOC100505582, LOC653052, PRO0593, Stank	homeodomain interacting protein kinase 2	Nucleus	kinase	28996	15258	362342
HMOX1	bK286B10, D8Wsu38e, haemox, HEME OXYGENASE, HEME OXYGENASE (DECYCLIZING) 1, Heme oxygenase 1, Hemox, Heox, HEOXG, Hmox, HMOX1D, HO-1, HSP32	heme oxygenase 1	Cytoplasm	enzyme	3162	15368	24451
IL36G	IL-1F9, IL-1H1, IL-1RP2, IL1E, interleukin 1 family, member 9, interleukin 36 gamma, interleukin 36 γ, interleukin 36, gamma, interleukin 36, γ, RGD1563019	interleukin 36 gamma	Extracellular Space	cytokine	56300	215257	499744
ME1	BRCAME, D9Ertd267e, HUMNDME, Malate Nadp Oxyreductase, Malic enzyme, malic enzyme 1, malic enzyme 1, NADP(+)-dependent, cytosolic, Mdh-1, MES, MOD1	malic enzyme 1	Cytoplasm	enzyme	4199	17436	24552
NQO1	AV001255, DHQU, DIA4, DT-diaphorase, DTD, NAD DT-diaphorase, NAD(P)H dehydrogenase, quinone 1, NAD(P)H quinone dehydrogenase 1, NAD(P)H:quinone oxidoreductase, Nadph dehydrogenase, Nadph diaphorase, Nadph Quinone Oxidoreductase-1, NMO1, NMOR, NMOR1, NMORI, Nqo, Ox-1, Qr, QR1, Quinone reductase	NAD(P)H quinone dehydrogenase 1	Cytoplasm	enzyme	1728	18104	24314
NR0B1	AHC, AHCH, AHX, DAX-1, DSS, GTD, HHG, NROB1, nuclear receptor subfamily 0 group B member 1, nuclear receptor subfamily 0, group B, member 1, SRXY2	nuclear receptor subfamily 0 group B member 1	Nucleus	ligand-dependent nuclear receptor	190	11614	58850
OSGIN1	1700012B18Rik, BDGI, OKL38, oxidative stress induced growth inhibitor 1	oxidative stress induced growth inhibitor 1	Other	growth factor	29948	71839	171493
PGD	0610042A05Rik, 6PGD, 6PGDH, AU019875, C78335, Cc2-27, LOC100363662, phosphogluconate dehydrogenase	phosphogluconate dehydrogenase	Cytoplasm	enzyme	5226	110208	100360180
PHGDH	3-PGDH, 3-phosphoglycerate dehydrogenase, 4930479N23, A10, HEL-S-113, NLS, NLS1, PDG, PGAD, PGD, PGDH, PGDH3, PHGDHD, phosphoglycerate dehydrogenase, SERA	phosphoglycerate dehydrogenase	Cytoplasm	enzyme	26227	236539	58835
POMP	2510048O06Rik, C13orf12, HSPC014, LOC100911238, PNAS-110, PRAAS2, proteasome maturation protein, proteasome maturation protein-like, RGD1305831, UMP1	proteasome maturation protein	Nucleus	other	51371	66537	288455 100911238
PRDX1	ENHANCER, Enhancer protein, Hbp23, MSP23, NKEF-A, OSF-3, PAG, PAGA, PAGB, PEROXIREDOXIN 1, peroxiredoxin 1-like 1, PEROXYREDOXIN 1, Prdx1l1, PrdxI, PRX1, PRXI, TDPX2, TDX2, TPxA	peroxiredoxin 1	Cytoplasm	enzyme	5052	18477	117254 100363379
PSAT1	D8Ertd814e, EPIP, NLS2, Phosphoserine Aminotransferase, phosphoserine aminotransferase 1, PSA, PSA1, PSAT, PSATD, Similar to phosphoserine aminotransferase	phosphoserine aminotransferase 1	Cytoplasm	enzyme	29968	107272	293820
PSMA4	20S PROTEASOME alpha 4 subunit, 20S PROTEASOME α 4 subunit, C9, HC9, HsT17706, Macropain subunit C9, proteasome (prosome, macropain) subunit, alpha type 4, proteasome (prosome, macropain) subunit, α type 4, proteasome subunit alpha 4, Proteasome subunit c9, proteasome subunit α 4, Proteosome subunit α 4, PSC9	proteasome subunit alpha 4	Cytoplasm	peptidase	5685	26441	29671
PSMA5	Aa409047, Macropain zeta chain, Macropain ζ chain, proteasome (prosome, macropain) subunit, alpha type 5, proteasome (prosome, macropain) subunit, α type 5, proteasome subunit alpha 5, proteasome subunit α 5, PSC5, ZETA, ζ	proteasome subunit alpha 5	Cytoplasm	peptidase	5686	26442	29672

SI Appendix Table S3: 46 NFE2L2 target gene transcripts from IPA(continue)

Symbol	Synonym(s)	Entrez Gene Name	Location	Family	Entrez Gene ID		
					Human	Mouse	Rat
PSMB2	AU045357, AW108089, beta 2 PROTEASOME subunit, C7-I, D4Wsu33e, HC7-I, proteasome (prosome, macropain) subunit, beta type 2, proteasome (prosome, macropain) subunit, β type 2, proteasome subunit beta 2, proteasome subunit β 2, β 2 PROTEASOME subunit	proteasome subunit beta 2	Cytoplasm	peptidase	5690	26445	29675
PSMB5	26s Proteasome Beta 5, 26s Proteasome β 5, beta 5 PROTEASOME subunit, Lmp17, LMPX, MB1, proteasome (prosome, macropain) subunit, beta type 5, proteasome (prosome, macropain) subunit, β type 5, Proteasome 20S X, proteasome subunit beta 5, proteasome subunit β 5, X proteasome subunit, β 5 PROTEASOME subunit	proteasome subunit beta 5	Cytoplasm	peptidase	5693	19173	29425
PSMD4	AF, AF-1, angiocidin, ASF, MCB1, proteasome (prosome, macropain) 26S subunit, non-ATPase, 4, Proteasome 26s subunit non-atpase 4, proteasome 26S subunit, non-ATPase 4, pUB-R5, Rpn10, S5A	proteasome 26S subunit, non-ATPase 4	Cytoplasm	other	5710	19185	83499
S100P	MIG9, PLACENTAL CALCIUM binding, S100 calcium binding protein P	S100 calcium binding protein P	Cytoplasm	other	6286		
SERPINE1	beta MIGRATING PLAS ACTIVATOR, beta-MIGRATING PLASMINOGEN ACTIVATOR INHIBITOR I, PAI, PAI-1, PAI1A, Pai1aa, Planh, PLANH1, Plasminogen activator inhibitor 1, RATPAI1A, serine (or cysteine) peptidase inhibitor, clade E, member 1, serpin family E member 1, SERPINE, β MIGRATING PLAS ACTIVATOR, β-MIGRATING PLASMINOGEN ACTIVATOR INHIBITOR I	serpin family E member 1	Extracellular Space	other	5054	18787	24617
SHC1	p52SHC, p66, P66shc, SHC, Shc (46 kDa isoform), SHC adaptor protein 1, Shc p66 isoform, SHCA, src homology 2 domain-containing transforming protein C1	SHC adaptor protein 1	Cytoplasm	other	6464	20416	85385
SHMT2	2700043D08Rik, AA408223, AA986903, GLYA, HEL-S-51e, serine hydroxymethyltransferase 2 (mitochondrial), Serine Hydroxymethyltransferase2, SHMT	serine hydroxymethyltransferase 2	Cytoplasm	enzyme	6472	108037	299857
SLC7A11	9930009M05RIK, AI451155, CCBR1, CYSTEINE GLUATAMINE TRANSPORTER, solute carrier family 7 (cationic amino acid transporter, y+ system), member 11, solute carrier family 7 member 11, sut, xCT	solute carrier family 7 member 11	Plasma Membrane	transporter	23657	26570	310392
SNAI2	SLUG, SLUGH, SLUGH1, snail family transcriptional repressor 2, snail family zinc finger 2, SNAIL2, WS2D	snail family transcriptional repressor 2	Nucleus	transcription regulator	6591	20583	25554
SOD1	ALS, ALS1, B430204E11Rik, Cu/Zn-SOD, CuZnSOD, czSOD, HEL-S-44, hSod1, Ipo-1, IPOA, SOD, SOD1L1, SODC, superoxide dismutase 1, superoxide dismutase 1, soluble	superoxide dismutase 1	Cytoplasm	enzyme	6647	20655	24786
SOD2	IMAGE:4711494, IPO-B, MANGANESE DEPENDENT SOD, Manganese Superoxide Dismutase, Manganese Superoxide Dismutase 2, MGC5618, MITOCHONDRIAL SOD, Mn superoxide dismutase, MNSOD, mtSOD, MVCD6, superoxide dismutase 2, superoxide dismutase 2, mitochondrial	superoxide dismutase 2	Cytoplasm	enzyme	6648	20656	24787
SRGN	haematoPOETIC PROTEOGLYCAN CORE, HEMATOPOETIC PROTEOGLYCAN CORE, PGSG, PPG, PRG, PRG1, Serglycin, Sgc	serglycin	Cytoplasm	other	5552		
TALDO1	TAL, TAL-H, TALDOR, Transaldolase, transaldolase 1	transaldolase 1	Cytoplasm	enzyme	6888	21351	83688
TFAM	AI661103, Hmgts, MTDPS15, MTTF1, MTTFA, TCF6, TCF6L1, TCF6L2, TCF6L3, Tfa, transcription factor A, mitochondrial, tsHMG	transcription factor A, mitochondrial	Cytoplasm	transcription regulator	7019	21780	83474
TKT	HEL-S-48, HEL107, p68, SDDHD, TK, TKT1, TRANSKETOLASE	transketolase	Cytoplasm	enzyme	7086	21881	64524
UGT1A1	BILIQTL1, BILIRUBIN UDP-GLUCURONOSYLTRANSFERASE ISOENZYME1, GNT1, HUG-BR1, UDP glucuronosyltransferase 1 family, polypeptide A1, UDP glucuronosyltransferase family 1 member A1, Udp Glycosyltransferase 1, UDPGT, UDPGT 1-1, Udpgt-1a, UGT1, UGT1A, UGT1A01, Ugt1a2b, UgtBr1	UDP glucuronosyltransferase family 1 member A	Cytoplasm	enzyme	54658	394436	24861
UGT1A7 (incl	A13, GNT1, HLUGP4, hUG-BR1, LOC100048744, LUGP4, mUGTBr/P, UDP glucuronosyltransferase 1 family, polypeptide A9, UDP glucuronosyltransferase family 1 member A10, UDP glucuronosyltransferase family 1 member A7, UDP glucuronosyltransferase family 1 member A8, UDP glucuronosyltransferase family 1 member A9, UDP glycosyltransferase 1 family, polypeptide A10, UDPGT, UDPGT 1-7, UDPGT 1-8, UDPGT 1-9, UGT-1A, UGT-1G, UGT-1H, UGT-1I, UGT-1J, UGT1, UGT1-01, UGT1-07, UGT1-08, UGT1-09, UGT1-10, UGT1-9, UGT1.1, UGT1.10, UGT1.8, UGT1.9, UGT1A1, UGT1A10, Ugt1a11, Ugt1a12, Ugt1a13, UGT1A8, UGT1A8S, UGT1A9, UGT1A9S, UGT1AI, UGTP4	UDP glucuronosyltransferase family 1 member A	Cytoplasm	enzyme	54577 54576 54575 54600	394434 394430	301595

SI Appendix Table S4. Antibodies used in the current study

Name of antibody	Vendor	Catalog no.	Dilution used
β-Catenin	Abcam	ab 16051	1:4000
CPT1A	Abcam	ab128568	1:1000
GAPDH	Sigma	G8795	1:10,000
GLUT1	Abcam	ab115730	1:20,000
Glut-Synthese	GeneTex	GTX109121	1:5000
Glutamate Dehydregenase	CST	12793	1:1000
Glutaminase	Abcam	ab131554	1:1000
c-Myc	Cell Signaling Tech	13987	1:1000
OXPHOS cocktail	Abcam	ab110413	1:1000
PAI1 (SerpinE1)	R&D	AF3828sp	1:1000
PCNA	Santa Cruz	SC-56	1:1000
PDH-E1α	Santa Cruz	SC-377092	1:1000
pPDH-E1α(pSer$_{293}$)	Calbiochem	AP1062	1:1000
p70 S6 Kinase	CST	2708	1:1000
pp70 S6 kinase(Thr389)	CST	97596	1:1000
YAP	CST	4912	1:1000